Boundary layer recovery and precipitation symmetrization preceding rapid intensification of tropical cyclones under shear

Article

Accepted Version

Chen, X., Gu, J.-F. ORCID: https://orcid.org/0000-0002-7752-4553, Zhang, J. A., Marks, F. D., Rogers, R. F. and Cione, J. J. (2021) Boundary layer recovery and precipitation symmetrization preceding rapid intensification of tropical cyclones under shear. Journal of the Atmospheric Sciences, 78 (5). pp. 1523-1544. ISSN 0022-4928 doi: 10.1175/jas-d-20-0252.1 Available at https://centaur.reading.ac.uk/96833/

To link to this article DOI: http://dx.doi.org/10.1175/jas-d-20-0252.1

Publisher: American Meteorological Society

Boundary Layer Recovery and Precipitation Symmetrization Preceding Rapid Intensification of Tropical Cyclones under Shear

Xiaomin Chen[1*], Jian-Feng Gu[2], Jun A. Zhang[1, 3], Frank D. Marks[1], Robert F. Rogers[1], and Joseph J. Cione[1]

[1]NOAA/AOML Hurricane Research Division, Miami, FL, USA

[2]Department of Meteorology, University of Reading, Reading, UK

[3]University of Miami, Cooperative Institute for Marine and Atmospheric Studies, Miami, FL, USA

Submitted to *Journal of the Atmospheric Sciences*

Revised by February 22, 2021

---

[*] Corresponding author: Dr. Xiaomin Chen (xiaomin.chen@noaa.gov)

Abstract

This study investigates the precipitation symmetrization preceding rapid intensification (RI) of tropical cyclones (TCs) experiencing vertical wind shear by analyzing numerical simulations of Typhoon Mujigae (2015) with warm (CTL) and relatively cool (S1) sea surface temperatures (SSTs). A novel finding is that precipitation symmetrization is maintained by the continuous development of deep convection along the inward flank of a convective precipitation shield (CPS), especially in the downwind part. Beneath the CPS, downdrafts flush the boundary layer with low-entropy parcels. These low-entropy parcels do not necessarily weaken the TCs; instead, they are "recycled" in the TC circulation, gradually recovered by positive enthalpy fluxes, and develop into convection during their propagation toward a downshear convergence zone. Along-trajectory vertical momentum budget analyses reveal the predominant role of buoyancy acceleration in the convective development in both experiments. The boundary layer recovery is more efficient for warmer SST, and the stronger buoyancy acceleration accounts for the higher probability of these parcels developing into deep convection in the downwind part of the CPS, which helps maintain the precipitation symmetrization in CTL. In contrast, less efficient boundary layer recovery and less upshear deep convection hinder the precipitation symmetrization in S1. These findings highlight the key role of boundary layer recovery in regulating the precipitation symmetrization and upshear deep convection, which further accounts for an earlier RI onset timing of the CTL TC. The inward rebuilding pathway also illuminates why deep convection is preferentially located inside the radius of maximum wind of sheared TCs undergoing RI.

Accepted for publication in *Journal of the Atmospheric Sciences*. DOI 10.1175/JAS-D-20-0252.1.

1. Introduction

Accurate forecasts of rapid intensification (RI) of tropical cyclones (TCs) remain a challenging task (DeMaria et al. 2014), especially under moderate vertical wind shear (VWS) (Bhatia and Nolan 2013). Whether and when a TC is going to undergo RI under moderate VWS depends crucially on the other environmental factors including sea surface temperature and environment humidity (Tao and Zhang 2014). This forecast challenge becomes even more acute for prelandfall RI forecasts. One recent example in point is Hurricane Michael (2018), which underwent an unexpected prelandfall RI[1] under moderate VWS and became a category-5 hurricane near landfall.

In the presence of VWS, dry TC-like vortices are usually vertically tilted (Jones 1995, 2004). When coupled with moist processes, the balanced mesoscale lifting associated with the tilted vortex organizes a convective precipitation shield (CPS) in the downtilt side (e.g., Wang and Holland 1996; Corbosiero and Molinari 2002; Reasor et al. 2013; Gu et al. 2019). Observational and modeling studies of early-stage TCs[2] under moderate VWS indicate a common feature before RI onset: as the midlevel TC vortex precesses from the downshear-left to upshear and the TC vortex becomes nearly vertically aligned, the CPS also propagates into the upshear flank and spirals inward toward the formation of an incipient eyewall (e.g., Rappin and Nolan 2012; Zhang and Tao 2013; Alvey et al. 2015; Rogers et al. 2016; Chen et al. 2017; Leighton et al. 2018; Rios-Berrios et al. 2018; Ryglicki et al. 2018). This process is also termed precipitation symmetrization. The radius of maximum wind (RMW) contracts inward significantly during the vortex alignment and precipitation symmetrization, as documented in

---

[1] The prelandfall RI means that the RI occurs within 1-2 days of landfall and the RI can last to the landfall time.

[2] Early-stage TCs include the tropical depressions, tropical storms, and Category-1 hurricanes.

previous studies (e.g., Judt and Chen 2016; Chen et al. 2018a, b; Miyamoto and Nolan 2018; Tang et al. 2019). The coupled inner-core structural and precipitation evolution preceding RI onset for TCs in shear indicates the necessity to examine these processes in an integrated framework before proposing a theoretical explanation for RI onset in shear.

The contribution of the deep convection in the CPS to vortex alignment has been examined in previous studies, and two different pathways have been proposed, either through the downshear reformation that involves a newly formed center (Molinari et al. 2004; Molinari et al. 2006; Nguyen and Molinari 2015; Chen et al. 2018b; Rogers et al. 2020) or through an inner-core vorticity "restructuring" process (Rios-Berrios et al. 2018; Miyamoto and Nolan 2018; Shimada and Horinouchi 2018). Both pathways involve sustained deep convection in the azimuthally-propagating CPS and continuous merger of convectively-induced vorticity anomalies. In an analytical study using a shallow-water model, Schecter (2020) demonstrated that the two different pathways mentioned above can be explained by the relative strength between the velocity-convergence generated by the mass sink on the downshear side (cf. the downshear convergence zone in Chen et al. 2018b) and a critical value that is determined by the horizontal scale of the mass sink as well as the absolute value of the drift velocity of the mass sink relative to the background cyclonic flow.

The linkage between the precipitation symmetrization and RMW contraction was also examined in a modeling study (Chen et al. 2018a). By performing a set of numerical simulations for Typhoon Mujigae (2015) over various sea surface temperatures (SSTs), Chen et al. (2018a) found that TCs over different SSTs all undergo vertical alignment and precipitation symmetrization before RI onset. However, over warmer SST TCs exhibit a higher degree of precipitation symmetry, and the RMW contraction and RI occur much earlier. Diagnoses using the Sawyer-Eliassen equation indicate that the stronger diabatic heating due to more midlevel and deep convection within the inner core (also within the CPS) contributes to the earlier RMW contraction of the TCs over warmer SST. These results are consistent with earlier analytical analyses invoking balanced dynamics in that diabatic heating near/inside of the RMW benefits the RMW contraction and TC intensification (Schubert and Hack 1982; Pendergrass and Willoughby 2009).

Given the pivotal role of deep convection in both vortex alignment and RMW contraction, understanding the mechanisms that maintain the deep convection in the CPS during precipitation symmetrization is key. Convective downdrafts can bring low-entropy air parcels into the boundary layer and cool the inflow layer (Tang and Emanuel 2010; Riemer et al. 2010; Zhang et al. 2013; Gu et al. 2015; Wadler et al. 2018b; Chen et al. 2019), i.e., the low-level ventilation, which is argued as the most detrimental pathway of VWS to weaken a TC (Riemer et al. 2010, 2013). The boundary layer recovery of these downdraft-cooled parcels by the surface enthalpy fluxes is argued as the key to compensate for the low-level ventilation and impacts the subsequent TC intensity change (Powell 1990; Tang and Emanuel 2012; Molinari et al. 2013; Zhang et al. 2017b; Zhang and Rogers 2019; Nguyen et al. 2019). However, the linkage between the boundary layer recovery and convective development in sheared TCs remains elusive: recent idealized simulations with the same SST attribute convective initiation in the azimuthally-propagating CPS before RI onset to dynamical forcing, rather than buoyancy forcing (Gu et al. 2019).

As a follow-up of Chen et al. (2018a), this study will further examine the numerical simulation dataset for Typhoon Mujigae (2015) over various SSTs. It is hypothesized that the boundary layer recovery is more effective under warmer SST conditions, and a comparison of two representative experiments with warm and relatively cool SSTs provides a unique opportunity to gain insight into the role of boundary layer recovery in governing the distribution of deep convection within the TC inner core, which is the key to further understand the relationship between precipitation symmetrization, RMW contraction, and RI onset for sheared TCs. The specific scientific questions to be addressed in this study include:

1) Before RI onset, how is the CPS organized and maintained during precipitation symmetrization under VWS?
2) What is the role of boundary layer recovery in the convective development and precipitation symmetrization?
3) What is the relative importance between dynamical and buoyancy forcing in the convective development?

The remainder of this paper is organized as follows. Section 2 describes the methods and simulation datasets used in this study. Section 3 provides an overview of the vortex intensity and structural change, and precipitation evolution prior to the RI onset in warm and relatively cool SST experiments. Section 4 compares the organization of the CPS during precipitation symmetrization in the two experiments. The role of boundary layer recovery in the convective development and precipitation symmetrization is discussed in section 5. Additional discussion and concluding remarks are given in sections 6 and 7, respectively.

2. Data and Methods

Following Chen et al. (2018a), the same two representative WRF-ARW experiments of Typhoon Mujigae (2015) with warm (CTL) and relatively cool (S1) SSTs are compared in this study. The model setup for these two experiments is the same except for the initial SST. In CTL, the SST is set as the initial condition at 0000 UTC 2 October, while in S1 the SST is set as the climatological monthly-mean state (MMSST) averaged from 1990 to 2013. The MMSST averaged in the South China Sea is 28.6°C, 1°C cooler than that in CTL. For simplicity, the ocean coupling is not included and the SST is not updated during the simulation in these experiments. The horizontal resolution of the triple-nested domains is 12, 4, and 1.33 km, respectively. The outermost domain is static and the inner two domains move with the simulated TC. All three domains contain 51 sigma levels with the top level at 50 hPa. The CTL simulation successfully captures the track, prelandfall RI, and storm structure evolution. In comparison, the RI onset timing lags by 13 h in the S1 experiment and the intensification rate is much weaker. For more details of model setup, verification, and differences in the two experiments, we refer interested readers to Chen et al. (2018a).

The objective partitioning method proposed by Rogers (2010) is adopted to separate the convective, stratiform, and other (typically flanking the stratiform) type precipitation. This method uses reflectivity criteria at 0.9 and 3 km heights and a threshold of vertical velocity averaged between 0.9 and 2.1 km (i.e., >0.5 m s^{-1}) to identify convective points. If one grid point is not flagged as a convective point and 3-km reflectivity is >20 dBZ, it is flagged as stratiform precipitation [for more details, see Rogers (2010)]. Then, based on the height of cloud top, indicated by 20-dBZ echo top, the convective region is further divided into shallow (< 4 km), midlevel (4-8 km), and deep (>8 km) convection following Fritz et al. (2016). We also pay attention to one type of extreme deep convection, namely convective bursts (CBs) and adopt the definition proposed by Rogers (2010). A CB is defined as a grid point where the layer-averaged vertical velocity within the 300–700-hPa layer exceeds 5 m s^{-1}.

A forward trajectory analysis is performed in section 5 to investigate the boundary layer recovery of the downdraft-cooled parcels. To compute the trajectory of air parcels ending in rapidly changing convection, output from the innermost domain is saved every 1 min. The parcels to be tracked are selected near the TC center and beneath the vortex-tilt-related CPS, and their trajectories over the analysis period do not cross the boundary of the innermost moving nest. The predictor-corrector technique is used for the trajectory calculation, following Onderlinde and Nolan (2016). The essence of this technique is to use the wind information at the predicted midpoint to advect the parcel at the initial location for a full-time step. The predicted midpoint is determined by advecting the parcel from the initial location by a half time step using the wind information at the initial location. The time step selected is 30s, since a higher temporal resolution produces similar results.

The TC center at a given pressure level is defined as the geopotential height centroid (Chen et al. 2018b), which is skillful at locating the TC center for weak storms (Nguyen et al. 2014). Vortex tilt is calculated as the distance between the TC centers at 450 hPa and 850 hPa pressure levels.

3. Overview of vortex intensity and structural change prior to RI onset

Typhoon Mujigae underwent RI over the warm water in the South China Sea under moderate VWS. The magnitude of 200-850 hPa VWS remained 7-8 m s^{-1} before RI onset[3] (i.e., 0000 UTC 3 October). Note that the 200–850-hPa VWS is calculated for the area between 200 and 800 km from the surface TC center. The VWS subsequently decreased to 4-5 m s^{-1} during the early RI period and then increased to 7-9 m s^{-1} near the end of RI, which was followed by the landfall near 0600 UTC 4 October. Both simulations have similar VWS evolution to observations. The CTL TC successfully reproduces the intensity evolution, and its RI lasts from

---

[3] RI onset in this study is defined as the time when the increase in 10-m maximum wind speed (VMAX) exceeds 15 m s^{-1} in the subsequent 24 h or shorter period, if the RI duration is less than 1 day. An additional requirement is that the VMAX should increase in the first 6 h of the subsequent 24-h or shorter period.

0000 UTC 3 October to 0300 UTC 4 October (Fig. 1a). In comparison, the RI onset of the S1 TC is delayed by 13 h. The RI duration of the S1 TC is ~14h, as the maximum surface wind increases from 29 m s^{-1} at 1300 UTC 3 October to 46 m s^{-1} at 0300 UTC 4 October.

In addition to the similar evolution of VWS in the two experiments, the CTL and S1 TCs undergo similar vertical alignment prior to RI onset, as the midlevel vortex gradually precesses from the downshear-left quadrant to upshear, and the magnitude of the 400-850 hPa TC vortex tilt decreases with time (Fig. 1b). However, the different RI onset timing between the two TCs suggests vertical alignment, albeit necessary, is not a sufficient RI indicator under moderate VWS. Instead, RI onset in both experiments is effectively indicated when the RMW contraction (Fig. 1d) reaches a certain threshold measured in terms of the local Rossby number at 10-m height (R_o > 12, Fig. 1c). The local Rossby number is defined as $R_o = v_m/(r_m f)$, where v_m is the maximum azimuthal mean tangential wind at 10-m height, r_m represents the RMW, and f represents the Coriolis parameter at the TC center. Of note, the R_o threshold (i.e., R_o > 12) cannot be overgeneralized beyond this case, which is latitude dependent based on its definition. Additionally, the value of R_o at RI onset varies by changing the size and intensity of the initial vortex, translational speed, and VWS magnitude (Miyamoto and Nolan 2018). Nonetheless, this metric shows that the CTL TC contracts much earlier and its RI starts much earlier too.

Figure 2 shows three snapshots of the simulated radar reflectivity and background horizontal convergence at 1.5-km height for the CTL and S1 experiments. Concurrent with vertical alignment, both TCs undergo precipitation symmetrization before RI onset. The background horizontal convergence is computed with the coarser data resolution of 0.5°× 0.5° that is interpolated from the outermost model domain with a horizontal resolution of 12 km, following Chen et al. (2018b). A mesoscale convergence zone exists in the downshear quadrants of both TCs, which is consistent with the findings in the simulated Typhoon Vicente (2012) (Chen et al. 2018b). The formation of the downshear convergence zone can be explained by the differential vorticity advection by VWS, which induces mesoscale lifting and low-level convergence in the downshear side (Bender 1997; Bracken and Bosart 2000). The convergence zone remains in the downshear side during precipitation symmetrization.

4. Inward rebuilding of CPS during precipitation symmetrization

In this section, we mainly focus on the comparison between CTL and S1 experiments over the 12-h period preceding the RI onset of the CTL TC (i.e., 1200 UTC 2 October−0000 UTC 3 October) following Chen et al. (2018a). This is the period when the RMW evolution differs between the two experiments (Fig. 1d), which further impacts the RI onset timing (Fig. 1a).

Figures 3a-d show the location of deep convection and CBs within r = 100 km in three consecutive 3-h periods at a 10-min interval after 1200 UTC 2 October. In both TCs, deep convection propagates azimuthally from downshear to upshear and meanwhile radially inward toward the TC center over the three periods. The evolution of CBs location over the same periods exhibits similar features in CTL, while the radially inward shift of CBs location is less notable in S1. In this study, *we define the inward rebuilding of the CPS as deep convection continuously develops at the inward flank and downwind part of the CPS during precipitation symmetrization*. The inward rebuilding process in these two experiments is a reminiscence of the "inward progression" of cloud-to-ground lightning clusters from large radii downshear to smaller radii upshear in RI TCs under moderate VWS (e.g., Molinari et al. 2004; Molinari and Vollaro 2010; Stevenson et al. 2014; Zawislak et al. 2016). The inward rebuilding is more notable in CTL, and the CTL TC has much more (1091) grid points of deep convection within the inner-core region (i.e., r = 60 km), particularly in the upshear side (Figs. 3a-b and 3e). The CTL TC also has 90 more CBs within the inner core (Fig. 3f), and the difference in the number of CBs between the two TCs is most prominent in the downshear-left quadrant. Nevertheless, the CTL TC has slightly more CBs in the upshear-left quadrant (see Figs. 3c-d and 3f). The difference in the deep convection or CBs in the upshear-left quadrant between the two experiments is consistent with previous observational studies that found deep convection in the upshear-left quadrant is key to determining subsequent intensity change (e.g., Wadler et al. 2018a).

An examination of the animation of radar reflectivity at the lowest model level indicates that the newly-developed deep convection related to inward rebuilding are mostly initiate in the downshear-left quadrant inside the RMW and mature along their path toward the downshear convergence zone (see the supplemental movie). Figure 4 presents two examples for the CTL and S1 TCs. In the CTL TC, a 40-50-km long spiral rainband (circled by a thick dashed line) is visible in the downshear-right quadrant at 1710 UTC 2 October (Figs. 4a-b). Of note, this spiral rainband is only visible below the lowest 1.5 km at this moment (not shown), suggesting that it remains in the boundary layer. This rainband gradually develops above the boundary layer and matures (>55 dBZ) during the propagation from the downshear-left to upshear-left quadrant (Figs. 4c-f). The 40-50-km long spiral rainband then becomes the leading edge of the azimuthally propagating CPS as preexisting convection weakens due to its own lifecycle, resulting in an inward rebuilding event. Figures 4g-l show a similar phenomenon occurring over a later period for the S1 TC, i.e., from 1920 UTC 2 October to 2030 UTC 2 October. A notable difference is that the newly-developed spiral rainband in the S1 TC is much weaker than that of the CTL TC in terms of the radar reflectivity. Thus, the convective activity at the downwind part of the CPS in S1 is weaker than that in CTL after this inward rebuilding event (Figs. 4k-l).

Accepted for publication in *Journal of the Atmospheric Sciences*. DOI 10.1175/JAS-D-20-0252.1.

Figure 5 further compares the composite vertical structure of the newly-developed deep convection between the CTL and S1 TCs over the period of inward rebuilding (see Fig. 4). Dashed lines in Figs. 5a-b mark the locations of the vertical slices in Figs. 5c-f. At $r = 50$ km, the maximum microphysics diabatic heating of the discrete convective tower within the 40-50 km long spiral rainband in CTL exceeds 40 K h^{-1} and the top of the strong diabatic heating (>40 K h^{-1}) extends to 11 km height (Fig. 5c), indicating that the newly-developed convection (Fig. 5a) is evolving toward its mature stage during its propagation toward the upshear-left quadrant (see Figs. 4d-f). In comparison, the strong diabatic heating (>40 K h^{-1}) of the newly-developed deep convection in S1 is vertically confined in the 5-8 km layer at $r = \sim58$ km. The region of larger value of absolute vorticity ($>0.5\times10^{-3}$ s^{-1}) outside of $r = 40$ km in S1 is ~4 km shallower than that in CTL (Figs. 5c-d).

The composite storm-relative streamlines in Figs. 5e-f indicate two sources of convective updrafts for the matured newly-developed deep convection within $r = 60$ km (Figs. 5e-f). The first source comes from the radial inflow jet ($\theta_e < 354$ K) that descends from the freezing level into the boundary layer, pass through the high-entropy ($\theta_e > 358$ K) central area within $r = 40$ km, and then becomes outflow above the boundary layer. The inflow to outflow transition is indicative of supergradient wind. The second source is directly traced back to the “eye” region within the lowest 2 km, which is closely related to the inward rebuilding process. Of note, the incipient eyewall with a clear eye appears 2 hours later than the composite period (e.g., Fig. 2c). A comparison of the red streamline in Figs. 5e-f demonstrates that the maximum height related to the second source of convective updrafts differs between the two experiments, as convective updrafts in CTL vertically extend to ~17 km height, 5 km taller than the updrafts in S1. These findings in Fig. 5 again suggest that the discrepancies in the strength of newly-developed deep convection inside of the RMW affect the convective activity at the downwind part of the azimuthally propagating CPS.

To systematically examine the outward propagation of newly-formed deep convection inside the RMW, Figure 6 shows the evolution of radar reflectivity azimuthally averaged within the downshear-right and downshear-left quadrants below 500-m height in CTL and S1. We only select the downshear quadrants, given that the newly-developed convection typically become visible in the boundary layer of the downshear-left quadrant and convection at the smaller radii in upshear-left may mask the signal of outward propagation of newly-formed deep convection toward the RMW (cf. Fig. 4). This averaging method can capture the distinct inward rebuilding events in which the newly-developed deep convection projects significantly onto the azimuthal mean. Figure 6 presents five and four visually trackable inward rebuilding events over the 12-h period before 0000 UTC 3 October for the CTL and S1 TCs, respectively. The S1 TC undergoes a notable inward rebuilding over 1600-1630 UTC (i.e., the event 1), with the maximum radar reflectivity comparable to that of the inward rebuilding events of the CTL TC. Nevertheless, the strength of outward propagating convection in terms of radar reflectivity is weaker in S1 than that in CTL on average. The outward propagation of the circled spiral rainband shown in Figs. 4a-f and Figs. 4g-l corresponds to the event 3 in Fig. 6a and Fig. 6b, respectively.

Figures 7a-b further assess the impact of inward rebuilding on precipitation symmetrization and show a time-azimuthal plot of the radar reflectivity averaged within the 20-50 km radii and within the 0-500 m layer for the CTL and S1 TCs, respectively. We select the annulus within the initial RMW (i.e., 60 km) to better illustrate the inward rebuilding of the CPS during precipitation symmetrization. The CPS in CTL spans a broader azimuthal coverage and generally exhibits a more vigorous convective activity in terms of radar reflectivity than the CPS in S1 over the 12-h period, and the latter is consistent with Fig. 6. Precipitation symmetrization in CTL is sustained with more vigorous convection over the 12-h period; however, precipitation symmetrization in S1 is only notable when the convective activity is most vigorous over 1600-1830 UTC (see the reflectivity maximum in Fig. 7b). These findings demonstrate that precipitation symmetrization is closely related to the strength of the outward propagating newly-developed deep convection inside the RMW (see also Figs. 4-6). Additionally, the relatively weak echo (10-25 dBZ) in the right-of-shear quadrants of the CTL TC is related to stratiform precipitation (see Figs. 8a-b). The area of stratiform precipitation substantially increases in the right-of-shear quadrants of the CTL TC while those quadrants of the S1 TC are almost devoid of stratiform precipitation, which can be inferred from the comparison between Figs. 7a and 7b and clearly seen from one example in Fig. 8.

A large patch of low-θ_e air (<358 K) at the lowest model level appears in the upshear-left quadrant near 1800 UTC 2 October and is superimposed by the downward motion (<-0.2 m s^{-1}) at 1-km height at the leading edge of the spiral rainband (Figs. 7c-d). This finding suggests that the low-θ_e air originates from above the boundary layer and is transported downward by convective downdrafts. This low-level ventilation pathway is comparable with the one proposed by Riemer et al. (2010), although they discussed this process in a mature hurricane with a well-defined eyewall. These low-θ_e parcels are then advected downwind and their θ_e gradually recover to higher values during their propagation toward the downshear-right quadrant (i.e., ~1800-2100 UTC 2 October), indicative of a boundary layer recovery process (Powell 1990; Molinari et al. 2013; Zhang et al. 2013; Nguyen et al. 2019). Multiple low-level ventilation and subsequent boundary layer recovery events can be found in both experiments over the 12-h period. In CTL, the θ_e averaged within the lowest 500 m is generally 2-K warmer than that in S1 (cf. Figs. 7c and 7d). Given the inward rebuilding events in CTL are generally stronger than those in S1, a key question arises as whether the stronger newly-developed deep convection in CTL is attributed to the more effective boundary layer recovery for the warmer SST. In the next section, we will address this issue by performing trajectory analyses and along-trajectory vertical momentum budgets.

5. Boundary layer recovery

a. Trajectory analyses

To examine the role of boundary layer recovery in the inward rebuilding process, a forward Lagrangian trajectory analysis of the downdraft-related low-θ_e air parcels in the lower boundary layer, beneath the leading edge of the CPS, is carried out. The 4-h trajectory analysis starts from 1700 UTC and 1740 UTC 2 October for the CTL and S1 TCs, respectively, when the midlevel vortex of both TCs is located upshear (Fig. 1b), and the pattern and intensity of the CPS (Figs. 9a and 9d) as well as the low-θ_e values beneath the rainband are comparable (Figs. 9b-c and 9e-f). Over the 4-h period, precipitation symmetrization is sustained in CTL while it is hindered after 1830 UTC 2 October in S1 (Figs. 7a-b). A total of 320 parcels are tracked from the low-θ_e region, with 64 parcels at 3rd, 5th, 7th, 9th, and 11th lowest model levels, respectively. The mean height of all of these 5 model levels is below 450 m. The initial locations of the 64 parcels at each model level are the same (see black dots in Figs. 9a and 9d), and the horizontal spacing between each parcel at the same model level is 4 km. Figures 9b-c and 9e-f show the initial trajectory points colored by the maximum height of the subsequent 4-h forward trajectories. The parcels with their maximum height below 1.5 km are referred to as “boundary layer parcels” (PBL). The others with their maximum height within 1.5-4 km, 4-8 km, and >8 km are grouped into shallow, midlevel, and deep convection categories, respectively, which is analogous to the partitioning of convection in section 2. A comparison of the parcel trajectories starting from the 3rd (Figs. 9b-c) and 7th (Figs. 9e-f) lowest model levels between CTL and S1 indicates that the parcels in CTL are more likely to develop into deep convection, while most of the parcels in S1 fail to escape from the boundary layer (<1.5 km). Similar results are also found for the trajectories starting from other model levels in the lower boundary layer (not shown). Statistics based on the maximum height of these 4-h trajectories confirm this statement (Fig. 10). More than 80% of the tracked parcels in CTL develop into convection while the ratio decreases ~40% in S1. Moreover, ~35% of these parcels in CTL develop into deep convection while the ratio decreases to <3% in S1. These results are consistent with the difference in the strength of inward rebuilding between the event 4 in CTL and event 3 in S1 (Fig. 6).

To quantitatively examine the differences in the trajectories between the two experiments, the top 20% of the tracked parcels based on their maximum height of the 4-h trajectory are selected for a comparison. Figure 11 shows the evolution of height and vertical velocity along the trajectories. Over the first 2 hours of the trajectories (t = 0-2 h), these parcels in both CTL and S1 generally stay below 1.5 km height, and their vertical velocity is generally <1 m s^{-1}. The parcel height evolution in CTL and S1 diverges afterwards (Fig. 11a), as the upward motion of these parcels in CTL accelerates more rapidly than that in S1 (Fig. 11b). Considering these facts, the boundary layer recovery of these parcels over t = 0-2 h is examined in Fig. 12. In CTL, the mean θ_e increase over t = 0-2 h for these parcels is ~5 K (Fig. 12a). In contrast, the mean θ_e increase in S1 is 1.5 K over the same period, which is 3.6 K lower than that in CTL. Figure 12b further shows that at t = 0 h the mean θ_e of these parcels in CTL is 2.1 K cooler than that in S1, while at t = 2 h the mean θ_e of these parcels in CTL is 1.5 K warmer. Additionally, the mean parcel height in both experiments is <600 m over t = 0-2 h, and mean parcel height in CTL is 190 m lower than that in S1 (Fig. 12a). Given that the period of trajectory analyses is before sunrise at local time (0100-0500 LST for CTL), there is no incoming shortwave radiation; in right-of-shear quadrants, weak radiative heating is only found in the boundary layer of the downshear-left quadrant and is one order smaller in magnitude than the diabatic heating due to upward enthalpy fluxes (not shown). Thus, the upward enthalpy fluxes from the ocean surface is the dominant energy source in the lower boundary layer; the more efficient boundary layer recovery in CTL is attributed to the warmer SST as well as the ability of these parcels to stay at a lower height where the upward enthalpy fluxes are typically larger (Zhang and Drennan 2012).

b. Along-trajectory vertical momentum budgets

To investigate the mechanisms responsible for the convective initiation and the subsequent convective development during precipitation symmetrization, a vertical momentum budget along the trajectories of the top 20% of the tracked parcels is performed for both experiments (Jeevanjee and Romps 2015):

$$\frac{dw}{dt} = a_i + a_b, \qquad (1)$$

in which *w* is the vertical velocity and the vertical acceleration ($\frac{dw}{dt}$) is decomposed into dynamic (a_i) and buoyancy (a_b) accelerations. The buoyancy acceleration (or “effective buoyancy”) is defined as the Lagrangian acceleration that would result if the wind were instantaneously zeroed out. Similarly, the dynamic acceleration is defined as the Lagrangian vertical acceleration resulting from an instantaneous zeroing out of any horizontal density anomalies. The relative roles of these two acceleration terms could be quantified by solving the Poisson equation:

$$-\nabla^2(\bar{\rho} a_b) = \mathrm{g}\nabla_\mathrm{h}^2 \rho, \qquad (2)$$

$$-\nabla^2(\bar{\rho} a_i) = -\,\partial_\mathrm{z} \nabla \cdot [\bar{\rho}(\mathbf{u} \cdot \nabla)\mathbf{u}]\ , \qquad (3)$$

Accepted for publication in *Journal of the Atmospheric Sciences*. DOI 10.1175/JAS-D-20-0252.1.

where $\bar{\rho}$ is horizontal average of air density in the budget domain, ρ is the air density, g is the gravitational acceleration, and $\mathbf{u}$ is the three-dimensional wind vector, ∇^2 is the three-dimensional Laplacian operator, and ∇_h^2 is the horizontal Laplacian operator. Dirichlet boundary conditions of $a_i = 0$ and $a_b = 0$ are specified on the top and bottom boundaries following Jeevanjee and Romps (2015). The main advantage of this form of vertical momentum budget over other forms (e.g., Zhang et al. 2000; Braun 2002; Eastin et al. 2005) is that it refrains from the ambiguity in the arbitrary definition of the reference state $\bar{\rho}$ when calculating the Archimedean buoyancy (Davies-Jones 2003; Doswell and Markowski 2004). Note that a_b includes both Archimedean buoyancy and the environment response to vertical acceleration driven by Archimedean buoyancy. To improve the accuracy of the interpolated vertical acceleration along the trajectories, the vertical momentum budget is performed from 50 m to 18 km height at a 50-m interval.

Figures 13a and 13d show that $\frac{dw}{dt}$ (=$a_i + a_b$) averaged below 1.5 km height and over t = 0-2 h is marginal in the right-of-shear semicircle. This finding is consistent with the fact that the top 20% of the tracked parcels stratified by their maximum height of the 4-h trajectory in both experiments stay in the boundary layer before arriving at the downshear convergence zone. The a_b within r = 40 km is positive in the right-of-shear semicircle below 1.5 km height (Figs. 13c and 13f), which is largely counteracted by a_i (Figs. 13b and 13e). The mean $\frac{dw}{dt}$ along the trajectory over t = 0-2 h is positive in both experiments (Fig. 14a). Of note, the mean w of the tracked parcels over the initial half hour is negative in both experiments (Fig. 11b), and negative $\frac{dw}{dt}$ is not required to retain these parcels in the boundary layer. The larger upward acceleration in S1 over t = 0-2 h is mainly attributed to the much larger a_b in S1 (Fig. 14a), which is further related to the smaller mean orbital radius (≈30 km) in S1 (Fig. 13) such that parcels can tap into the warm reservoir near the TC center (see Fig. 5e-f). In contrast, the mean orbital radius in CTL is 50 km, which is generally outside the region of relatively large a_b (>0.2 m s^{-2}).

The smaller mean $\frac{dw}{dt}$ over t=0-2 h in CTL (Fig. 14a) accounts for the lower mean parcel height in CTL than in S1 (Fig. 12a). These parcels subsequently arrive at the inward flank of the CPS, indicated by the spiral band of upward motion at 1.5 km height (Fig. 15), or downshear convergence zone, where both the dynamic and buoyancy forcing play an important role in lifting the parcels out of the boundary layer (i.e., convective initiation). The upward dynamic forcing is likely attributed to the low-level convergence in the downshear convergence zone, and it is difficult to further decompose the dynamical forcing to quantify the relative contribution of the low-level convergence and other mechanisms. The role of dynamic forcing in the convective initiation in the incipient eyewall is consistent with the findings in previous modeling studies of TCs (Zhang et al. 2000; Braun 2002; Gu et al. 2019). *One new finding in this study is that the buoyancy forcing also plays a role in the convective initiation at the inward flank of the CPS* (Figs. 15c and 15f). Figures 15 and 11 also indicate a striking difference between the two experiments: in CTL a large portion of these parcels have already developed or are going to develop into deep convection in the downwind part of the azimuthally-propagating CPS, as seen in Figs. 4-6, while in S1 the parcels reaching the downwind part of the CPS mostly develop into shallow and midlevel convection.

Figure 14b shows the vertical acceleration terms averaged over t = 2-3 h for the top 20% of the tracked parcels. Both the a_b and $\frac{dw}{dt}$ are significantly larger than those over t=0-2 h (Fig. 14a). Clearly, the acceleration of the upward motion above the boundary layer is mainly attributed to the a_b in both experiments. Parcels in CTL exhibit larger mean a_b over t = 2-3 h than those in S1, which is mainly attributed to the stronger a_b over t = 2.5-3 h in CTL (see Fig. 16). In S1, a_i

plays a secondary role in accelerating the upward motion; whereas in CTL, the mean a_i for these parcels is negative (Fig. 14b). Figure 16 further shows that in both experiments dynamic forcing accelerates the upward motion of parcels over t = 2-2.5 h, when these parcels still reside at low levels; as convection matures over t = 2.5-3 h, these parcels experience substantial dynamic deceleration. The dynamical deceleration in CTL is more notable over t = 2.5-3 h, leading to a net negative value of a_i over t = 2-3 h in CTL (Fig. 14b). The dynamical deceleration comes from the effect of a downward-pointing perturbation pressure gradient force (cf. Braun 2002). In short, the stronger acceleration of the upward motion during the convective development in CTL is attributed to the stronger a_b. Given the a_b during convective development is closely related to the θ_e values of the parcels at convective initiation, the above findings confirm that the boundary layer recovery of the downdraft-cooled parcels is a key mechanism in maintaining the convective activity during precipitation symmetrization.

6. Discussion

a. Observational support and additional discussions on precipitation symmetrization

As mentioned in section 4, the successive inward rebuilding of the CPS during precipitation symmetrization under moderate VWS is reminiscent of the observed “inward progression” of the cloud-to-ground lightning clusters in the RI TCs under moderate VWS (e.g., Molinari et al. 2004; Molinari and Vollaro 2010; Stevenson et al. 2014; Zawislak et al. 2016). Note that cloud-to-ground lightning can be treated as an indicator of strong/deep convection. These observational case studies clearly show that during precipitation symmetrization the lightning cluster drifted cyclonically from downshear-left at *large* radii to upshear-left at *smaller* radii and mostly inside the RMW. The relationship between boundary layer recovery and convective development in the sheared TCs was also alluded to in observational studies of Tropical Storm Edouard (2002) (Molinari et al. 2013), Hurricane Cristobal and Bertha (2014) (Nguyen et al. 2017), and early-stage TCs from 1997 to 2017 (see fig. 16 in Nguyen et al. 2019). These observational facts imply that the identified “inward rebuilding” pathway is not limited to one single sheared TC, and the related the dynamical (e.g., downshear convergence zone and the associated low-level convergence) and thermodynamic processes (e.g., boundary layer recovery) are intrinsic to sheared early-stage TCs.

Previous observational studies (e.g., Molinari et al. 2013; Nguyen et al. 2017) generally recognized that the high-θ_e parcels in the downshear-right quadrant contribute to the convective development in the left-of-shear quadrants of sheared TCs. However, to our knowledge, no direct evidence has been presented to prove that the downshear-right high-θ_e parcels that contribute to the subsequent left-of-shear convective development are an outcome of the boundary layer recovery of downdraft-cooled parcels beneath the CPS at earlier times. Thus, one unique contribution of this study is that the identified “inward rebuilding” pathway directly relates the boundary layer recovery of downdraft-cooled parcels to the development of deep convection in the left-of-shear quadrants. Additionally, observational and modeling studies of TCs in shear frequently pointed out the deep convection in the upshear quadrant and inside the RMW as a key factor in differentiating the RI and non-RI TCs (e.g., Rogers et al. 2016; Hazelton et al. 2017; Wadler et al. 2018a; Leighton et al. 2018), while mechanisms responsible for the radius and quadrant preference of deep convection for RI TCs remain elusive. The “inward rebuilding” pathway provides a reasonable explanation to this phenomenon. This pathway is considered applicable to the sheared TCs at tropical storm or minimal hurricane stage, when the eyewall has not yet typically formed, but when RI occurs more frequently (Kaplan et al. 2010; Chen et al. 2015).

Over warm SST, the CTL TC also has a much larger area of stratiform precipitation in the right-of-shear quadrants than the S1 TC after 1800 UTC 2 October (Figs. 7a-b, 8, and 17a-b). Figure 17 shows azimuthal-height plots of radar reflectivity, θ_e, relative humidity, and vertical velocity averaged within r = 20-60 km and over the period of 1800-1850 UTC 2 October for the CTL and S1 TCs. Given stratiform precipitation is preferred in an environment with high saturation fraction (López and Raymond 2005), the prevailing stratiform precipitation in the right-of-shear quadrants of the CTL TC suggest the inner-core environment therein is very moist, as seen from the nearly saturated 5-9 km layer above the freezing level (cf. Figs. 17c-d). In contrast, the RH of the 5-9 km layer in the right-of-shear quadrants of the S1 TC is <85%. An idealized simulation study (Rios-Berrios et al. 2018) also found that the right-of-shear quadrants of the TC inner core become very moist before RI onset. The humidification of the layer above the freezing level in the right-of-shear quadrants is most likely attributed to the horizontal advection of water vapor and the evaporation/sublimation of condensates coming from the upwind quadrants (Rappin and Nolan 2012; Alvey et al. 2020). All of these processes are closely related to the convection that transports the boundary layer moisture upward into the mid-to-upper troposphere. The left-of-shear convective activity within the inner core is generally more vigorous in CTL than in S1 over the 12-h period preceding the RI onset of the CTL TC (Figs. 7a-b), which helps account for the more moist midlevels in the right-of-shear quadrants of the CTL TC. In the numerical simulation study of Typhoon Vicente (2012), the amount of deep convection in upshear quadrants steadily increases 5 hours before RI onset (Chen et al. 2018b) and a nearly-saturated inner core forms at RI onset (Chen et al. 2019), which lends support to the hypothesis. A detailed diagnostic analysis of the moistening processes in a shear-relative framework is beyond the scope of this study and will be left for future work.

b. Comparison with a mesoscale convective system with trailing stratiform

The analyses in section 5 demonstrate that the precipitation symmetrization of the sheared TCs is essentially a three-dimensional rather than an axisymmetric process (also see Fig. 18). Particularly, the boundary layer recovery of downdraft-cooled parcels and the subsequent inward rebuilding of deep convection in the sheared TCs cannot be described in the simulations using an axisymmetric framework. Before the formation of a complete eyewall, the CPS propagates cyclonically and radially inward during precipitation symmetrization. The CPS in a sheared early-stage TC is analogous to a midlatitude mesoscale convective system with trailing stratiform (hereafter MCS-TS, Parker and Johnson 2000) in both morphology and organization, with ascending flow in the front (radially inward in a TC) of the moving MCS-TS and descending inflow from the rear (radially outward in a TC) and below the freezing level (Fig. 18d).

However, the CPS in a sheared TC differs from MCS-TS due to its imposed swirling circulation of the TC. In the mature stage of MCS-TS, convective updrafts are sustained by the high-θ_e inflow in the front, and the cold pool (i.e., low-θ_e) region remains in the rear flank of the convective system that induces low-level convergence for the convective updrafts. In a sheared TC, however, the downdraft-induced low-θ_e parcels are “recycled” in the TC circulation, gradually recovered by positive enthalpy fluxes, slowly ascend in the boundary layer (e.g., see the newly-formed spiral rainband along the trajectory in Fig. 18a) during their advection toward the downshear convergence zone, and ultimately become a part of the ascending branch radially inward of the downwind part of the CPS if their entropy has been sufficiently recovered. This scenario is seen in both TCs (Figs. 18b-e), while the newly-developed convection in the inward rebuilding events is weaker in the S1 TC. This conceptual model in Fig. 18 highlights the critical role of warm SST and boundary layer recovery in replenishing these low-θ_e parcels and favoring the symmetrization of the CPS in the sheared TCs prior to the formation of a closed eyewall.

An important implication of this study is that the low-level ventilation does not necessarily weaken the early-stage TCs over warm SSTs; instead, the competition between the low-level ventilation and boundary layer recovery matters to the subsequent convective activity and structural/intensity change of the early-stage TCs in VWS.

7. Concluding remarks

Precipitation symmetrization or eyewall formation preceding the rapid intensification (RI) of tropical cyclones (TCs) under moderate vertical wind shear (VWS) has been documented in recent studies (e.g., Zagrodnik and Jiang 2014; Tao and Jiang 2015; Alvey et al. 2015; Tao et al. 2017; Chen et al. 2017; Fischer et al. 2018). Understanding thermodynamic/dynamical mechanisms controlling the precipitation symmetrization is the central question addressed in this study. By analyzing two representative numerical simulations of Typhoon Mujigae (2015), initialized with warm (i.e., CTL) and relatively cool (i.e., S1) SSTs, respectively, key results are summarized as follows:

1) A downshear convergence zone forms due to the differential advection by the VWS. The convective precipitation shield (CPS) is initially embedded in this convergence zone and subsequently propagates into the upshear side before RI onset. Downdraft-cooled parcels beneath the CPS are advected downwind by the swirling winds and their entropy is gradually recovered by positive enthalpy fluxes (i.e., boundary layer recovery).

2) The boundary layer recovery is key to the convective development and precipitation symmetrization before RI onset. Trajectory analyses of the downdraft-cooled parcels and the

along-trajectory vertical momentum budget demonstrate that the boundary layer recovery is more efficient in CTL due to the warmer SST, and the resulting stronger buoyancy acceleration are responsible for the development of much more deep convection in CTL than in S1, particularly in the upshear quadrants. Additionally, downdraft-cooled parcels are lifted out of the boundary layer by both dynamical and buoyancy acceleration in the convergence zone (i.e., convective initiation).

3) The precipitation symmetrization before RI onset in both experiments is maintained by the continuous development of deep convection radially inward of the azimuthally propagating CPS (i.e., inward rebuilding event), as deep convection matures in the downwind part of the CPS. In CTL, precipitation symmetrization is sustained by stronger newly-developed deep convection in successive inward rebuilding events, and the associated stronger microphysics diabatic heating inside/near the radius of the maximum wind (RMW) aids in the earlier RMW contraction of the CTL TC (see discussions in Chen et al. 2018a). In contrast, precipitation symmetrization is delayed in S1 due to the weaker newly-developed convection radially inward of the CPS, particularly in the upshear-left quadrant, and the RMW contraction is also delayed.

These above processes form a positive feedback between boundary layer recovery, *inward rebuilding of the CPS*, precipitation symmetrization, and RMW contraction under the warmer SST, and highlight the key role of the boundary layer recovery of the downdraft-cooled parcels in alleviating the low-level ventilation and organizing the CPS during precipitation symmetrization. Additionally, these results provide an explanation for the frequently observed deep convection in the upshear quadrant and inside the RMW of the sheared TCs before RI onset.

Acknowledgments: This research had been supported by the National Key R&D Program of China under Grant 2017YFC1501601, the Natural Science Foundation of China Grants

41875067 and 41605033. We want to acknowledge Drs. Jon Zawislak, Andy Hazelton, and Paul Reasor for their helpful suggestions to the early version of the paper. Discussions with Prof. Juan Fang and Dr. Michael Fischer also provided valuable insight into the analysis. The first author Xiaomin Chen is supported by the NRC Research Associateship Programs. Jun A. Zhang is supported by NOAA grant NA14NWS4680030 and NSF grant AGS-1822128.

References

Alvey III, G. R., J. Zawislak, and E. Zipser, 2015: Precipitation properties observed during tropical cyclone intensity change. *Mon. Wea. Rev.*, **143**, 4476-4492.

Alvey, G. R., III, E. Zipser, and J. Zawislak, 2020: How does Hurricane Edouard (2014) evolve toward symmetry before rapid intensification? A high-resolution ensemble study. *J. Atmos. Sci.*, **77,** 1329-1351.

Bhatia, K. T., and D. S. Nolan, 2013: Relating the skill of tropical cyclone intensity forecasts to the synoptic environment. *Wea. Forecasting,* **28,** 961-980.

Bender, M. A., 1997: The effect of relative flow on the asymmetric structure in the interior of hurricanes. *J. Atmos. Sci.*, **54**, 703-724.

Bracken, W. E., and L. F. Bosart, 2000: The role of synoptic-scale flow during tropical cyclogenesis over the North Atlantic Ocean. *Mon. Wea. Rev.*, **128,** 353-376.

Braun, S. A., 2002: A cloud-resolving simulation of hurricane bob (1991): Storm structure and eyewall buoyancy. *Mon. Wea. Rev.*, **130,** 1573-1592.

Chen, X., Y. Wang, and K. Zhao, 2015: Synoptic flow patterns and large-scale characteristics associated with rapidly intensifying tropical cyclones in the South China Sea. *Mon. Wea. Rev.*, **143,** 64-87.

Chen, X., M. Xue, and J. Fang, 2018a: Rapid intensification of Typhoon Mujigae (2015) under different sea surface temperatures: Structural changes leading to rapid intensification. *J. Atmos. Sci.*, **75,** 4313-4335.

Chen, X., J. A. Zhang, and F. D. Marks, 2019: A thermodynamic pathway leading to rapid intensification of tropical cyclones in shear. *Geophys. Res. Lett.*, **46,** 9241-9251.

Chen, X., Y. Wang, K. Zhao, and D. Wu, 2017: A numerical study on rapid intensification of Typhoon Vicente (2012) in the South China Sea. Part I: Verification of simulation, storm-scale evolution, and environmental contribution. *Mon. Wea. Rev.*, **145,** 877-898.

Chen, X., Y. Wang, J. Fang, and M. Xue, 2018b: A numerical study on rapid intensification of Typhoon Vicente (2012) in the South China Sea. Part II: Roles of inner-core processes. *J. Atmos. Sci.*, **75,** 235-255.

Corbosiero, K. L., and J. Molinari, 2002: The effects of vertical wind shear on the distribution of convection in tropical cyclones. *Mon. Wea. Rev.*, **130,** 2110-2123.

Davies-Jones, R., 2003: An expression for effective buoyancy in surroundings with horizontal density gradients. *J. Atmos. Sci.*, **60**, 2922-2925.

DeMaria, M., C. R. Sampson, J. A. Knaff, and K. D. Musgrave, 2014: Is tropical cyclone intensity guidance improving? *Bull. Am. Meteorol. Soc.*, **95,** 387-398.

Doswell, C. A., and P. Markowski, 2004: Is buoyancy a relative quantity? Mon. Wea. Rev., 132, 853–863.

Eastin, M. D., W. M. Gray, and P. G. Black, 2005: Buoyancy of convective vertical motions in the inner core of intense hurricanes. Part II: Case studies. *Mon. Wea. Rev.*, **133,** 209-227.

Fischer, M. S., B. H. Tang, K. L. Corbosiero, and C. M. Rozoff, 2018: Normalized convective characteristics of tropical cyclone rapid intensification events in the north atlantic and eastern north pacific. Mon. Wea. Rev., 146, 1133-1155.

Fritz, C., Z. Wang, W. Nesbitt Stephen, and J. Dunkerton Timothy, 2016: Vertical structure and contribution of different types of precipitation during Atlantic tropical cyclone formation as revealed by TRMM PR. *Geophys. Res. Lett.*, **43,** 894-901.

Gu, J.-F., Z.-M. Tan, and X. Qiu, 2015: Effects of vertical wind shear on inner-core thermodynamics of an idealized simulated tropical cyclone. *J. Atmos. Sci.*, **72**, 511-530.

Accepted for publication in *Journal of the Atmospheric Sciences*. DOI 10.1175/JAS-D-20-0252.1.

Gu, J.-F., Z.-M. Tan, and X. Qiu, 2019: Intensification variability of tropical cyclones in directional shear flows: Vortex tilt–convection coupling. *J. Atmos. Sci.*, **76,** 1827-1844.

Jeevanjee, N., and D. M. Romps, 2015: Effective buoyancy, inertial pressure, and the mechanical generation of boundary layer mass flux by cold pools. *J. Atmos. Sci.*, **72,** 3199-3213.

Jones, S. C., 1995: The evolution of vortices in vertical shear. I: Initially barotropic vortices. *Quart. J. Roy. Meteor. Soc.*, **121,** 821-851.

−−, 2004: On the ability of dry tropical-cyclone-like vortices to withstand vertical shear. *J. Atmos. Sci.*, **61,** 114-119.

Judt, F., and S. S. Chen, 2016: Predictability and dynamics of tropical cyclone rapid intensification deduced from high-resolution stochastic ensembles. *Mon. Wea. Rev.*, **144,** 4395-4420.

Kaplan, J., M. DeMaria, and J. A. Knaff, 2010: A revised tropical cyclone rapid intensification index for the Atlantic and Eastern North Pacific basins. *Wea. Forecasting*, **25,** 220-241.

Leighton, H., S. Gopalakrishnan, J. A. Zhang, R. F. Rogers, Z. Zhang, and V. Tallapragada, 2018: Azimuthal distribution of deep convection, environmental factors, and tropical cyclone rapid intensification: A perspective from HWRF ensemble forecasts of Hurricane Edouard (2014). *J. Atmos. Sci.*, **75,** 275-295.

López Carrillo, C., and D. J. Raymond, 2005: Moisture tendency equations in a tropical atmosphere. *J. Atmos. Sci.*, **62,** 1601-1613.

Miyamoto, Y., and D. S. Nolan, 2018: Structural changes preceding rapid intensification in tropical cyclones as shown in a large ensemble of idealized simulations. *J. Atmos. Sci.*, **75,** 555-569.

Molinari, J., and D. Vollaro, 2010: Rapid intensification of a sheared tropical storm. *Mon. Wea. Rev.*, **138,** 3869-3885.

Molinari, J., D. Vollaro, and K. L. Corbosiero, 2004: Tropical cyclone formation in a sheared environment: A case study. *J. Atmos. Sci.*, **61,** 2493-2509.

Molinari, J., J. Frank, and D. Vollaro, 2013: Convective bursts, downdraft cooling, and boundary layer recovery in a sheared tropical storm. *Mon. Wea. Rev.*, **141,** 1048-1060.

Molinari, J., P. Dodge, D. Vollaro, K. L. Corbosiero, and F. Marks, 2006: Mesoscale aspects of the downshear reformation of a tropical cyclone. *J. Atmos. Sci.*, **63,** 341-354.

Nguyen, L. T., and J. Molinari, 2015: Simulation of the downshear reformation of a tropical cyclone. *J. Atmos. Sci.*, **72,** 4529-4551.

Nguyen, L. T., J. Molinari, and D. Thomas, 2014: Evaluation of tropical cyclone center identification methods in numerical models. *Mon. Wea. Rev.*, **142,** 4326-4339.

Nguyen, L. T., R. F. Rogers, and P. D. Reasor, 2017: Thermodynamic and kinematic influences on precipitation symmetry in sheared tropical cyclones: Bertha and Cristobal (2014). *Mon. Wea. Rev.*, **145**, 4423-4446.

Nguyen, L. T., R. Rogers, J. Zawislak, and J. A. Zhang, 2019: Assessing the influence of convective downdrafts and surface enthalpy fluxes on tropical cyclone intensity change in moderate vertical wind shear. *Mon. Wea. Rev.*

Onderlinde, M. J., and D. S. Nolan, 2016: Tropical cyclone–relative environmental helicity and the pathways to intensification in shear. *J. Atmos. Sci.*, **73,** 869-890.

Parker, M. D., and R. H. Johnson, 2000: Organizational modes of midlatitude mesoscale convective systems. *Mon. Wea. Rev.*, **128,** 3413-3436.

Pendergrass, A. G., and H. E. Willoughby, 2009: Diabatically induced secondary flows in tropical cyclones. Part I: Quasi-steady forcing. *Mon. Wea. Rev.*, **137,** 805-821.

Accepted for publication in *Journal of the Atmospheric Sciences*. DOI 10.1175/JAS-D-20-0252.1.

Powell, M. D., 1990: Boundary layer structure and dynamics in outer hurricane rainbands. Part II: Downdraft modification and mixed layer recovery. *Mon. Wea. Rev.*, **118,** 918-938.

Rappin, E. D., and D. S. Nolan, 2012: The effect of vertical shear orientation on tropical cyclogenesis. *Quart. J. Roy. Meteor. Soc.*, **138,** 1035-1054.

Reasor, P. D., R. Rogers, and S. Lorsolo, 2013: Environmental flow impacts on tropical cyclone structure diagnosed from airborne Doppler radar composites. *Mon. Wea. Rev.*, **141,** 2949-2969.

Riemer, M., M. T. Montgomery, and M. E. Nicholls, 2010: A new paradigm for intensity modification of tropical cyclones: Thermodynamic impact of vertical wind shear on the inflow layer. *Atmos. Chem. Phys.*, **10,** 3163-3188.

—, 2013: Further examination of the thermodynamic modification of the inflow layer of tropical cyclones by vertical wind shear. *Atmos. Chem. Phys.*, **13,** 327-346.

Rios-Berrios, R., C. A. Davis, and R. D. Torn, 2018: A hypothesis for the intensification of tropical cyclones under moderate vertical wind shear. *J. Atmos. Sci.*, **75,** 4149-4173.

Rogers, R., 2010: Convective-scale structure and evolution during a high-resolution simulation of tropical cyclone rapid intensification. *J. Atmos. Sci.*, **67,** 44-70.

Rogers, R. F., J. A. Zhang, J. Zawislak, H. Jiang, G. R. Alvey, E. J. Zipser, and S. N. Stevenson, 2016: Observations of the structure and evolution of Hurricane Edouard (2014) during intensity change. Part II: Kinematic structure and the distribution of deep convection. *Mon. Wea. Rev.*, **144,** 3355-3376.

Rogers, R. F., P. D. Reasor, J. A. Zawislak, and L. T. Nguyen, 2020: Precipitation processes and vortex alignment during the intensification of a weak tropical cyclone in moderate vertical shear. *Mon. Wea. Rev.*, **148**, 1899-1929.

Ryglicki, D. R., J. D. Doyle, Y. Jin, D. Hodyss, and J. H. Cossuth, 2018: The unexpected rapid intensification of tropical cyclones in moderate vertical wind shear. Part II: Vortex tilt. *Mon. Wea. Rev.*, **146,** 3801-3825.

Schecter, D. A., 2020: Distinct intensification pathways for a shallow-water vortex subjected to asymmetric "diabatic" forcing. *Dyn. Atmos. Oceans*, 101156.

Schubert, W. H., and J. J. Hack, 1982: Inertial stability and tropical cyclone development. *J. Atmos. Sci.*, **39,** 1687-1697.

Shimada, U., and T. Horinouchi, 2018: Reintensification and eyewall formation in strong shear: A case study of Typhoon Noul (2015). *Mon. Wea. Rev.*, **146,** 2799-2817.

Stevenson, S. N., K. L. Corbosiero, and J. Molinari, 2014: The convective evolution and rapid intensification of Hurricane Earl (2010). *Mon. Wea. Rev.*, **142,** 4364-4380.

Tang, B., and K. Emanuel, 2010: Midlevel ventilation's constraint on tropical cyclone intensity. *J. Atmos. Sci.*, **67,** 1817-1830.

—, 2012: Sensitivity of tropical cyclone intensity to ventilation in an axisymmetric model. *J. Atmos. Sci.*, **69,** 2394-2413.

Tang, X., Z.-M. Tan, J. Fang, E. B. Munsell, and F. Zhang, 2019: Impact of the diurnal radiation contrast on the contraction of radius of maximum wind during intensification of Hurricane Edouard (2014). *J. Atmos. Sci.*, **76,** 421-432.

Tao, C., and H. Jiang, 2015: Distributions of shallow to very deep precipitation–convection in rapidly intensifying tropical cyclones. *J. Clim.*, **28,** 8791-8824.

Tao, C., H. Jiang, and J. Zawislak, 2017: The relative importance of stratiform and convective rainfall in rapidly intensifying tropical cyclones. *Mon. Wea. Rev.*, **145,** 795-809.

Tao, D., and F. Zhang, 2014: Effect of environmental shear, sea-surface temperature, and ambient moisture on the formation and predictability of tropical cyclones: An ensemble-mean perspective. *J. Adv. Model. Earth Syst.*, **6,** 384-404.

Wadler, J. B., R. F. Rogers, and P. D. Reasor, 2018a: The relationship between spatial variations in the structure of convective bursts and tropical cyclone intensification as determined by airborne Doppler radar. *Mon. Wea. Rev.*, **146,** 761-780.

Wadler, J. B., J. A. Zhang, B. Jaimes, and L. K. Shay, 2018b: Downdrafts and the evolution of boundary layer thermodynamics in Hurricane Earl (2010) before and during rapid intensification. *Mon. Wea. Rev.*, **146,** 3545-3565.

Wang, Y., and G. J. Holland, 1996: Tropical cyclone motion and evolution in vertical shear. *J. Atmos. Sci.*, **53,** 3313-3332.

Zagrodnik, J. P., and H. Jiang, 2014: Rainfall, convection, and latent heating distributions in rapidly intensifying tropical cyclones. *J. Atmos. Sci.*, **71,** 2789-2809.

Zawislak, J., H. Jiang, G. R. Alvey, E. J. Zipser, R. F. Rogers, J. A. Zhang, and S. N. Stevenson, 2016: Observations of the structure and evolution of Hurricane Edouard (2014) during intensity change. Part I: Relationship between the thermodynamic structure and precipitation. *Mon. Wea. Rev.*, **144,** 3333-3354.

Zhang, D.-L., Y. Liu, and M. K. Yau, 2000: A multiscale numerical study of hurricane andrew (1992). Part III: Dynamically induced vertical motion. *Mon. Wea. Rev.*, **128,** 3772-3788.

Zhang, F., and D. Tao, 2013: Effects of vertical wind shear on the predictability of tropical cyclones. *J. Atmos. Sci.*, **70,** 975-983.

Zhang, J. A., and W. M. Drennan, 2012: An observational study of vertical eddy diffusivity in the hurricane boundary layer. *J. Atmos. Sci.*, **69,** 3223-3236.

Zhang, J. A., and R. F. Rogers, 2019: Effects of parameterized boundary layer structure on hurricane rapid intensification in shear. *Mon. Wea. Rev.*, **147**, 853-871.

Zhang, J. A., R. F. Rogers, P. D. Reasor, E. W. Uhlhorn, and F. D. Marks, 2013: Asymmetric hurricane boundary layer structure from dropsonde composites in relation to the environmental vertical wind shear. *Mon. Wea. Rev.*, **141,** 3968-3984.

Zhang, J. A., J. J. Cione, E. A. Kalina, E. W. Uhlhorn, T. Hock, and J. A. Smith, 2017b: Observations of infrared sea surface temperature and air–sea interaction in Hurricane Edouard (2014) using GPS dropsondes. *J. Atmos. Oceanic Technol.*, **34,** 1333-1349.

Zipser, E.J., 1969: The role of organized unsaturated convective downdrafts in the structure and rapid decay of an equatorial disturbance. *J. Appl. Meteor.*, **8**, 799–814.

Accepted for publication in *Journal of the Atmospheric Sciences*. DOI 10.1175/JAS-D-20-0252.1.

Table 1: Experiment descriptions.

	Description
CTL	Initialized with the SST at 0000 UTC October 2, 2015.
S1	Initialized with the 1990-2013 monthly-mean SST.

Figure captions

Fig. 1. Verification of simulated 10-m maximum wind speed (m s^{-1}) in the CTL (red) and S1 (black) experiments against the best track data of China Meteorological Administration (gray line with circles). (b) Evolution of the 450-850 hPa vortex tilt magnitude (km) for the CTL and S1 TCs from 1200 UTC 2 October to 1200 UTC 4 October. The three dashed lines mark the downshear-left (DL), upshear-left (UL), and upshear-right (UR) quadrants that the tilt vector points toward. Evolution of (c) local Rossby number R_o and (d) RMW (km) at 10-m height for the CTL and S1 TCs. The gray line in (c) denotes $R_o = 12$. The red (black) arrows in each panel denote the RI onset timing of CTL (S1) TC. Adapted from Chen et al. (2018a).

Fig. 2. (a)-(c) The 1.5-km radar reflectivity (shading; dBZ), background horizontal convergence (dashed contours with values of $-2.0, -1.0, -0.5\times10^{-4}$ s^{-1}), and storm-relative winds (vector, m s^{-1}) at (a) 1600 UTC 2 October, (b) 1800 UTC 2 October, and (c) 2100 UTC 2 October in CTL. (d)-(f) As in (a)-(c), but for S1.

Fig. 3. (a)-(b) The location of deep convection within r = 100 km relative to the surface TC center (black star) occurred over 1200-1500 UTC 2 October (black plus), 1500-1800 UTC 2 October (blue plus), and 1800-2100 UTC 2 October (red plus) in CTL and S1, respectively. (c)-(d) As in (a)-(b), but for the location of CBs. The black arrow in (a)-(d) denotes the 300-850 hPa vertical wind shear. Azimuthal distribution of the number of (e) grid points of deep convection and (f) CBs in CTL (red) and S1 (black) within r = 60 km accumulated over 1200-2100 UTC 2 October at a 10-min interval. The total number of deep convection and CBs in CTL and S1 are shown as texts. The shear-relative quadrants are labeled in each panel. DR, UR, UL, and DL denote downshear-right, upshear-right, upshear-left and downshear-left quadrant, respectively.

Fig. 4. (a)-(f) Evolution of radar reflectivity (shading, dBZ) and storm-relative wind (vector, m s^{-1}) at the lowest model level for the CTL TC from 1710 UTC 2 October to 1830 UTC 2 October. (g)-(l) As in (a)-(f), but for the S1 TC from 1920 UTC 2 October to 2030 UTC 4 October. The solid black circle denote the 50-km reference radius. The dashed black ellipse tracks the propagation of the developing convection inside of the RMW. The reference vector is shown in (a). The gray arrow on the top right corner denotes the heading of 200-850 hPa VWS.

Fig. 5. (a)-(b) Plan view of radar reflectivity (shading, dBZ) and storm-relative wind (vector, m s^{-1}) at the lowest model level at 1800 UTC 2 October for the CTL and at 2000 UTC 2 October for the S1 TC, respectively. (c)-(d) Composite vertical slice of microphysics diabatic heating (shading, K h^{-1}) and absolute vorticity (contoured at 0.5, 1, and 2×10^{-3} s^{-1}) over 1800-1850 UTC 2 October and over 2000-2050 UTC 2 October for the CTL and S1 TCs, respectively; (e)-(f) As in (c)-(d), but for θ_e (shading, K) and storm-relative wind (streamline). The position of the vertical slice in (c)-(f) is marked as black dash line in (a)-(b). The white arrow in (a)-(d) marks the location of the newly-formed deep convection. The red streamline in (e)-(f) is related to the newly-developed deep convection inside the RMW.

Fig. 6. (a)-(b) Time-radius plot of radar reflectivity (shading, dBZ) averaged azimuthally within the downshear quadrants and below 500 m height from 1200 UTC 2 October to 0000 UTC 3 October for the CTL and S1 TCs, respectively. The black dashed lines in each panel

denote the visually trackable outward propagation of newly-formed convection within the RMW.

Fig. 7. (a)-(b) Time-azimuthal plot of radar reflectivity (shading, dBZ) for the CTL and S1 TCs, respectively. (c)-(d) As in (a)-(b), but for θ_e (shading, K) and vertical velocity (contours with values of –0.2, 0.2, and 0.5 $\mathrm{m\ s^{-1}}$ and negative values are dashed) for the two TCs. The radar reflectivity and θ_e are averaged within r = 20-50 km and below 500-m height. The vertical velocity is averaged within r = 20-50 km at 1-km height. The solid white line denotes the heading direction of 200-850 hPa VWS. The dashed white line marks the shear-relative quadrants, as labeled at the bottom of each panel. DR, UR, UL, and DL denote downshear-right, upshear-right, upshear-left and downshear-left quadrant, respectively.

Fig. 8. Plan view of (a) radar reflectivity (shading, dBZ) at 3-km height and (b) precipitation mode at 1830 UTC 2 October. The red, yellow, and purple area in (b) denote convective, stratiform, and other type precipitation, respectively. (c)-(d) As in (a)-(b), but for S1 TC. The solid black arrow in (a)-(d) denotes the heading direction of 200-850 hPa VWS.

Fig. 9. Plan view of (a) radar reflectivity (shading, dBZ) at the 3rd lowest model level, θ_e (shading, K) at the (b) 3rd and (c) 7th lowest model levels at 1700 UTC 2 October for the CTL TC. (d)-(f) As in (a)-(c), but for the S1 TC at 1740 UTC. The location of the initial points of the trajectories are shown as black dots in (a) and (d), and are shown as colored dots based on the maximum height of the subsequent 4-h forward trajectory in (b)-(c) and (e)-(f). Black cross (×) denotes the boundary layer parcels with the maximum height <1.5 km. Pink, red, and violet dots denote the maximum height of these parcels within 1.5-4 km, 4-8 km, and >8 km, respectively. The large black dot at (0, 0) marks the surface TC center. The black circle represents the RMW near the surface. The orange box in (a) and (e) denotes the same area of (b)-(c) and (e)-(f), respectively. The mean height of each model level is shown in the title of each panel.

Fig. 10. Bar plot of the ratio of the track parcels that remain in the boundary layer (gray) or develop into the shallow (pink), midlevel (red) and deep (purple) convection in the CTL and S1 experiments.

Fig. 11. The evolution of (a) parcel height (km) and (b) vertical velocity ($\mathrm{m\ s^{-1}}$) along the 4-h trajectory for the top 20% of the parcels that are stratified by their maximum height of the 4-h trajectory. The red and gray lines denote the trajectories in CTL and S1, respectively.

Fig. 12. Statistics for the top 20% of the parcels stratified by their maximum height of the 4-h trajectory. (a) Mean parcels height during t = 0-2 h and differences in the mean θ_e from t = 0 h to t = 2 h in CTL (red) and S1 (gray). (b) Differences in the mean θ_e between CTL and S1 (CTL–S1) at t = 0 h and t = 2 h.

Fig. 13. Plan view of the (a) a_i (dynamic acceleration) + a_b (buoyancy acceleration) (shading, $\times10^{-3}\ \mathrm{m\ s^{-2}}$), (b) a_i, and (c) a_b averaged in the lowest 1.5 km layer and over t = 0-2 h in CTL. Contours denote 1.5-km vertical velocity with values of –1, –0.5, –0.2, 0.5, 1.0, 1.5, and 2.0 $\mathrm{m\ s^{-1}}$ (negative values dashed) averaged over the same period. (d)-(f) As in (a)-(c) but in S1. The 0-2 h storm-relative trajectories of the top 20% of the parcels that are stratified by their maximum height of the 4-h trajectory are overlaid. The black arrow in the upper-right corner denotes the heading direction of the 200-850 hPa VWS. The red crosses in each panel denote the starting points of these trajectories.

Fig. 14. Vertical velocity budget terms a_i, a_b , and $a_i + a_b$ (shading, $\times10^{-3}\ \mathrm{m\ s^{-2}}$) averaged over (a) t = 0-2 h and (b) t = 2-3 h for the top 20% of the parcels that are stratified by their maximum height of the 4-h trajectory.

Fig. 15. As in Fig. 13, but for the results over *t*=2-3 h.

Fig. 16. Evolution of vertical velocity budget terms a_i (blue), a_b (red), and $a_i + a_b$ (black) over *t* = 2-3 h for the top 20% of the parcels that are stratified by their maximum height of the 4-h trajectory in (a) CTL and (b) S1. Lines represent mean values; shading extends from minimum to maximum at each minute. The unit of the budget terms is 10^{-3} m s^{-2}.

Fig. 17. Azimuthal-height plot of radar reflectivity (shading, dBZ) and vertical velocity (contours with values of –0.4, –0.2, –0.1, 0.2, 0.5, 1.0, and 2.0 m $s^{-1,}$ negative values dashed) averaged within *r* =20-60 km and over 1800-1850 UTC 2 October for the (a) CTL and (b) S1 TCs. (c)-(d) As in (a)-(b), but shading denotes relative humidity (%). The vertical dashed white line marks the shear-relative quadrants, as labeled at the top of each panel. DR, UR, UL, and DL denote downshear-right, upshear-right, upshear-left and downshear-left quadrant, respectively.

Fig. 18. Conceptual model for the inward rebuilding and precipitation symmetrization under different SSTs. (a) Plan view of the CPS that propagates into the upshear-left (UL) quadrant. Beneath the CPS, downdraft-cooled parcels in the boundary layer subsequently undergo boundary layer recovery and develop into convection during their propagation toward the downshear quadrants. (b)-(c) As in (a), but at a later time before the RI onset of the CTL TC over warm SSTs. In (b), the more efficient boundary layer recovery and more notable inward building of deep convection in UL maintain the precipitation symmetrization over warm SSTs; the stratiform in the right-of-shear semicircle in (b) indicates a nearly-saturated layer above the freezing level. (c) Over relatively cool SSTs, newly-developed convection in the inward rebuilding events is much weaker, which hinders precipitation symmetrization. Reflectivity contours represent the CPS and convective cells. The red dashed arrow in (a)-(c) denotes the trajectory along which boundary layer recovery and the subsequent inward rebuilding occur. (d)-(e) Composite vertical cross-sections of reflectivity and streamlines over warm and relatively cool SSTs, respectively. Locations of the cross sections are marked as thick black lines in (b)-(c).

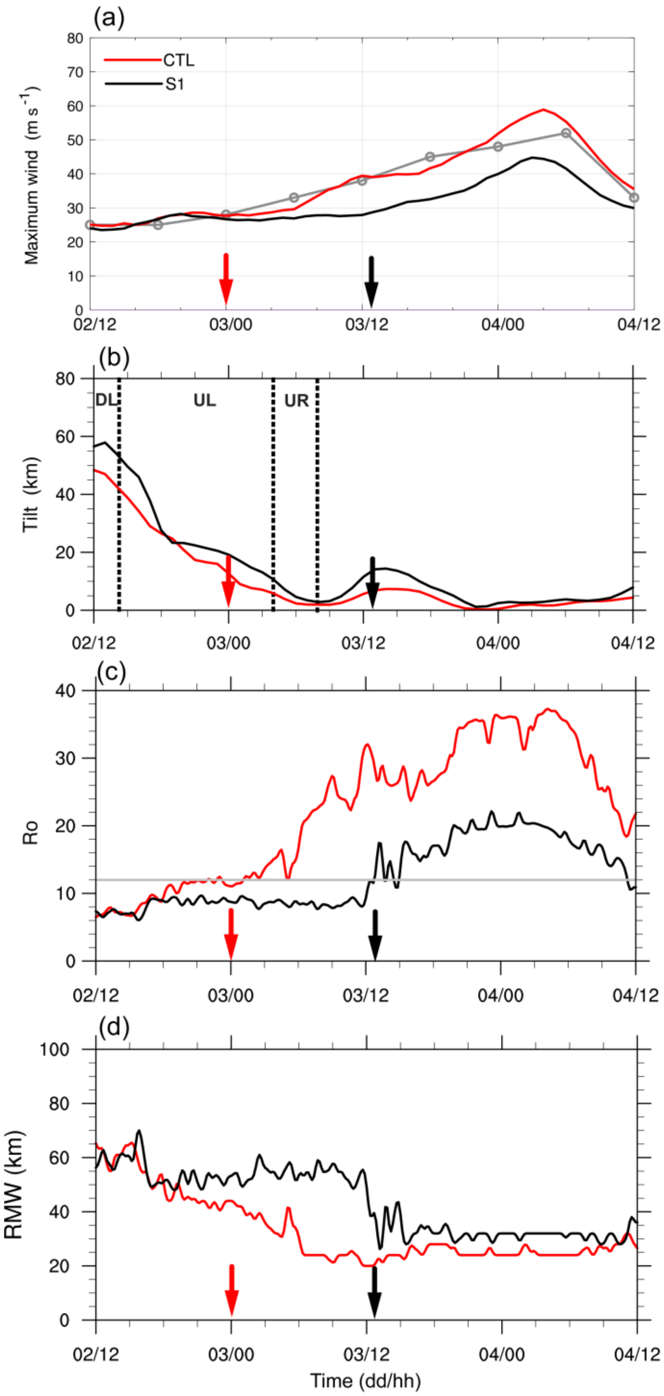

Fig. 1. Verification of simulated 10-m maximum wind speed (m s^{-1}) in the CTL (red) and S1 (black) experiments against the best track data of China Meteorological Administration (gray line with circles). (b) Evolution of the 450-850 hPa vortex tilt magnitude (km) for the CTL and S1 TCs from 1200 UTC 2 October to 1200 UTC 4 October. The three dashed lines mark the downshear-left (DL), upshear-left (UL), and upshear-right (UR) quadrants that the tilt vector points toward. Evolution of (c) local Rossby number R_o and (d) RMW (km) at 10-m height for the CTL and S1 TCs. The gray line in (c) denotes $R_o = 12$. The red (black) arrows in each panel denote the RI onset timing of CTL (S1) TC. Adapted from Chen et al. (2018a).

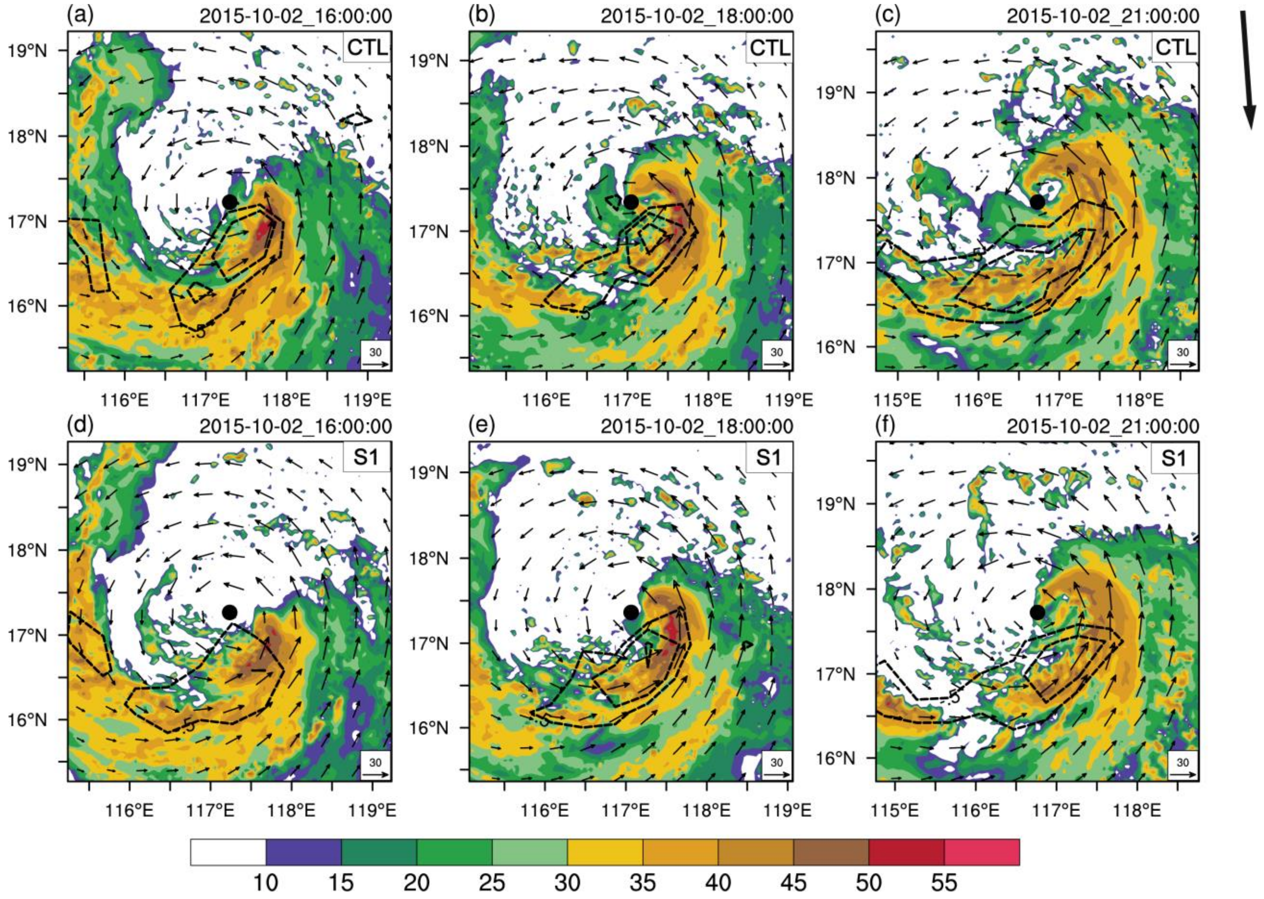

Fig. 2. (a)-(c) The 1.5-km radar reflectivity (shading; dBZ), background horizontal convergence (dashed contours with values of –2.0, –1.0, -0.5×10^{-4} s^{-1}), and storm-relative winds (vector, m s^{-1}) at (a) 1600 UTC 2 October, (b) 1800 UTC 2 October, and (c) 2100 UTC 2 October in CTL. (d)-(f) As in (a)-(c), but for S1.

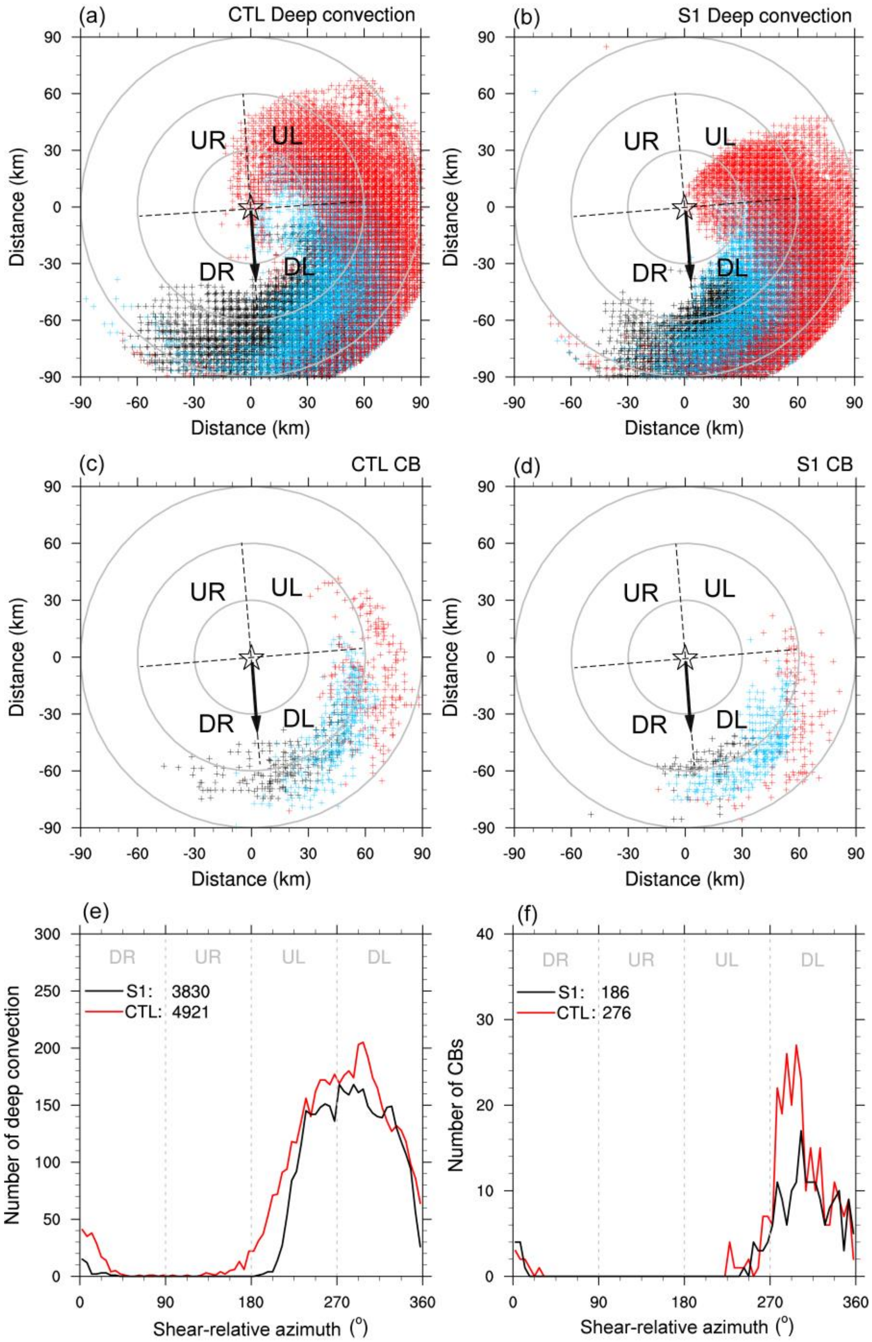

Fig. 3. (a)-(b) The location of deep convection within r = 100 km relative to the surface TC center (black star) occurred over 1200-1500 UTC 2 October (black plus), 1500-1800 UTC 2 October (blue plus), and 1800-2100 UTC 2 October (red plus) in CTL and S1, respectively. (c)-(d) As in (a)-(b), but for the location of CBs. The black arrow in (a)-(d) denotes the 300-850 hPa vertical wind shear. Azimuthal distribution of the number of (e) grid points of deep convection and (f) CBs in CTL (red) and S1 (black) within r = 60 km accumulated over 1200-2100 UTC 2 October at a 10-min interval. The total number of deep convection and CBs in CTL and S1 are shown as texts. The shear-relative quadrants are labeled in each panel. DR, UR, UL, and DL denote downshear-right, upshear-right, upshear-left and downshear-left quadrant, respectively.

Accepted for publication in *Journal of the Atmospheric Sciences*. DOI 10.1175/JAS-D-20-0252.1.

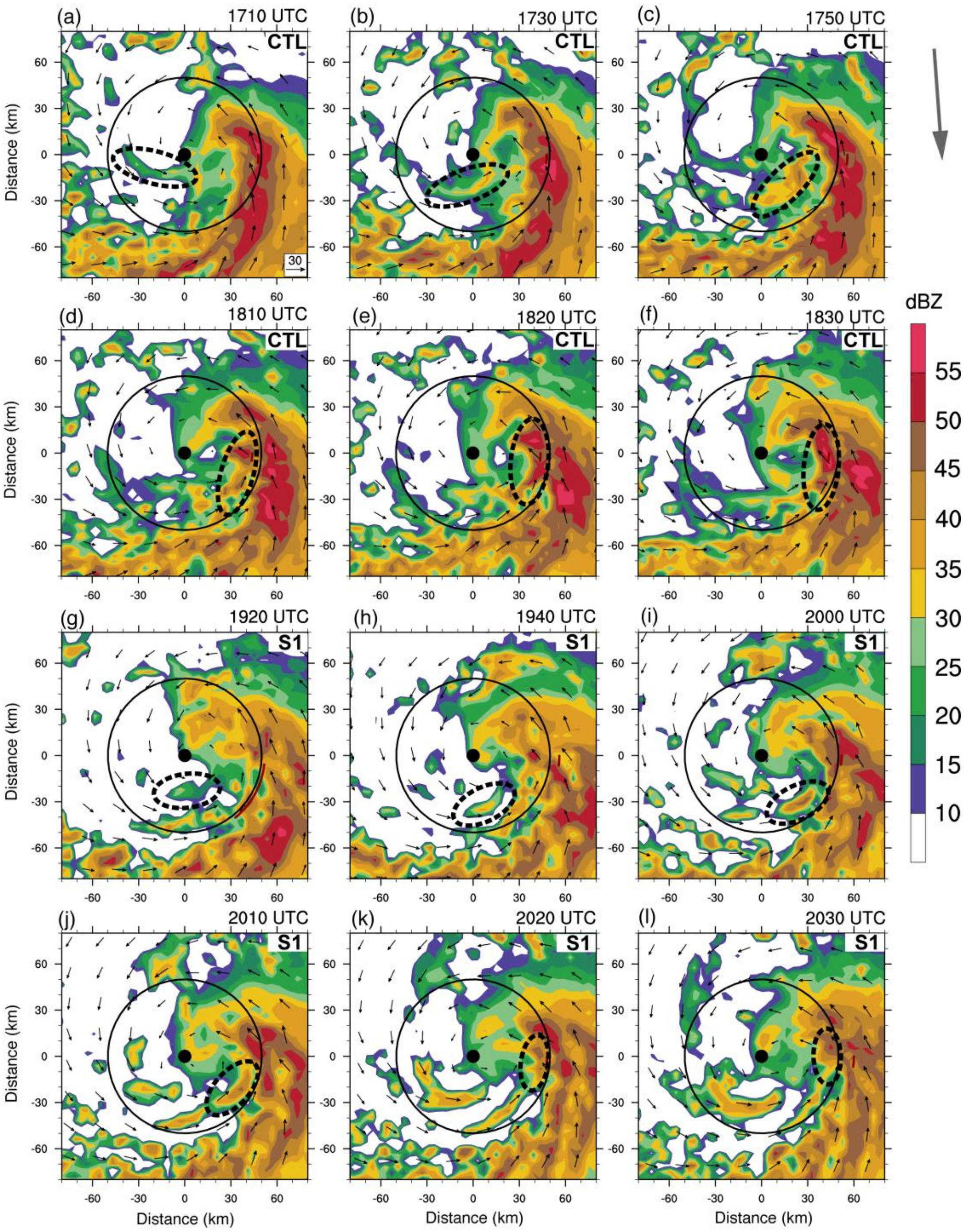

Fig. 4. (a)-(f) Evolution of radar reflectivity (shading, dBZ) and storm-relative wind (vector, m s^{-1}) at the lowest model level for the CTL TC from 1710 UTC 2 October to 1830 UTC 2 October. (g)-(l) As in (a)-(f), but for the S1 TC from 1920 UTC 2 October to 2030 UTC 4 October. The solid black circle denotes the 50-km reference radius. The dashed black ellipse tracks the propagation of the developing convection inside of the RMW. The reference vector is shown in (a). The gray arrow on the top right corner denotes the heading of 200-850 hPa VWS.

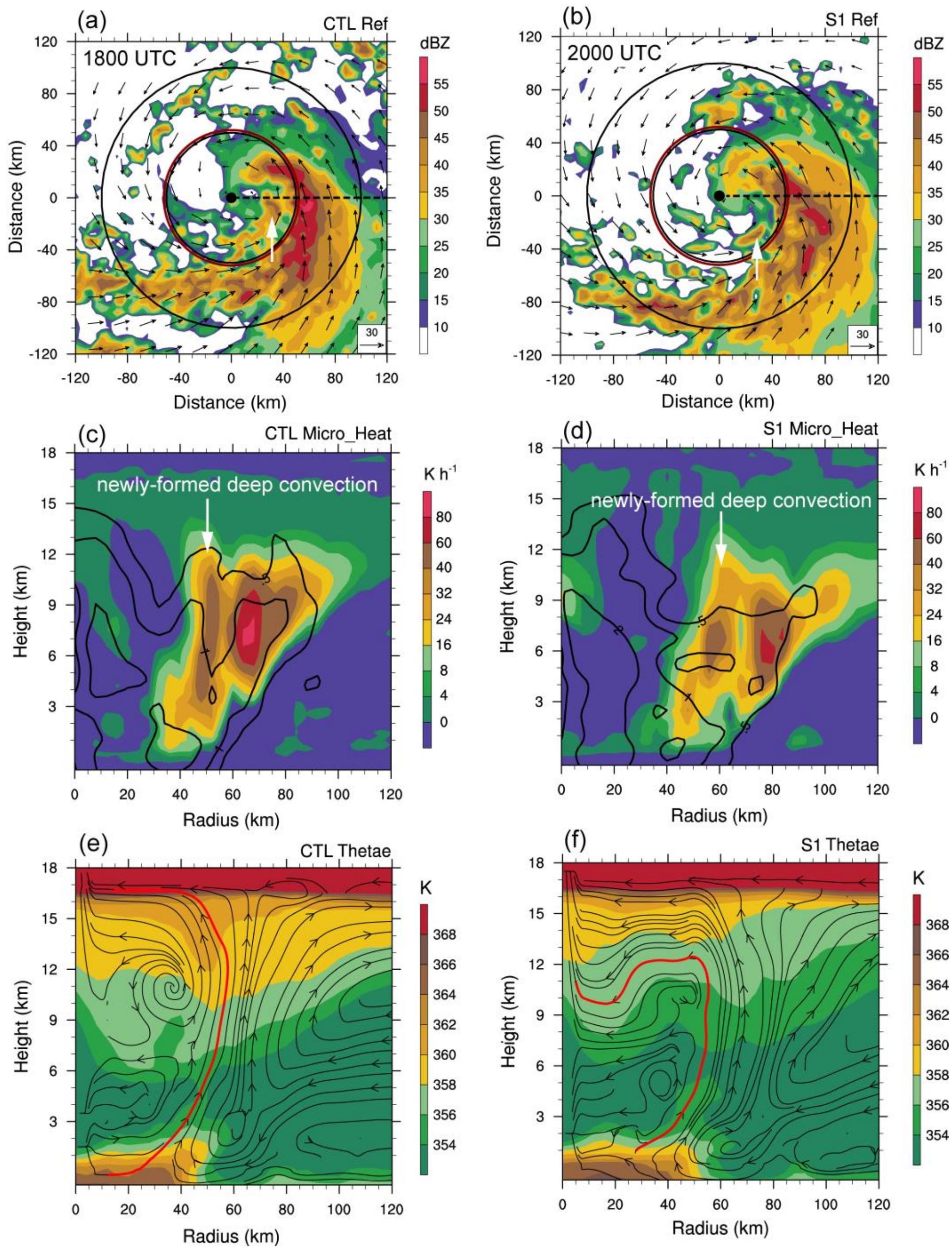

Fig. 5. (a)-(b) Plan view of radar reflectivity (shading, dBZ) and storm-relative wind (vector, m s^{-1}) at the lowest model level at 1800 UTC 2 October for the CTL and at 2000 UTC 2 October for the S1 TC, respectively. (c)-(d) Composite vertical slice of microphysics diabatic heating (shading, K h^{-1}) and absolute vorticity (contoured at 0.5, 1, and 2×10^{-3} s^{-1}) over 1800-1850 UTC 2 October and over 2000-2050 UTC 2 October for the CTL and S1 TCs, respectively; (e)-(f) As in (c)-(d), but for θ_e (shading, K) and storm-relative wind (streamline). The position of the vertical slice in (c)-(f) is marked as black dash line in (a)-(b). The white arrow in (a)-(d) marks the location of the newly-formed deep convection. The red streamline in (e)-(f) is related to the newly-developed deep convection inside the RMW.

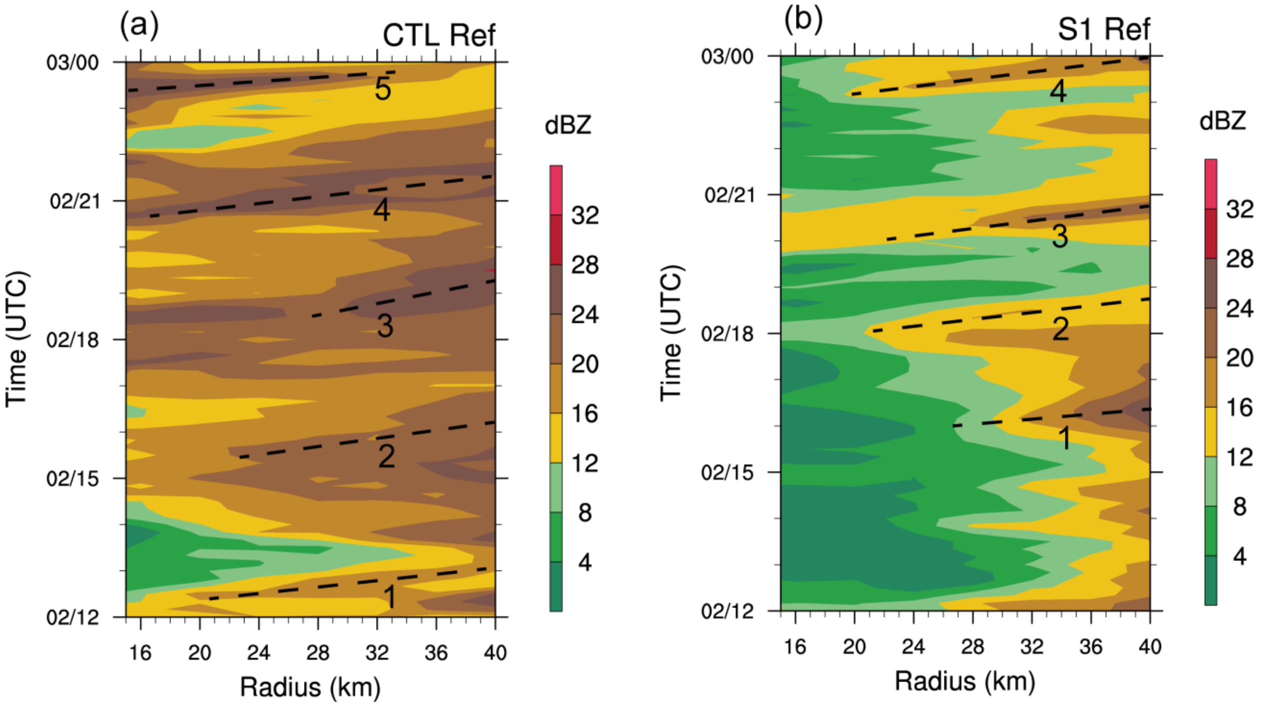

Fig. 6. (a)-(b) Time-radius plot of radar reflectivity (shading, dBZ) averaged azimuthally within the downshear quadrants and below 500 m height from 1200 UTC 2 October to 0000 UTC 3 October for the CTL and S1 TCs, respectively. The black dashed lines in each panel denote the visually trackable outward propagation of newly-formed convection within the RMW.

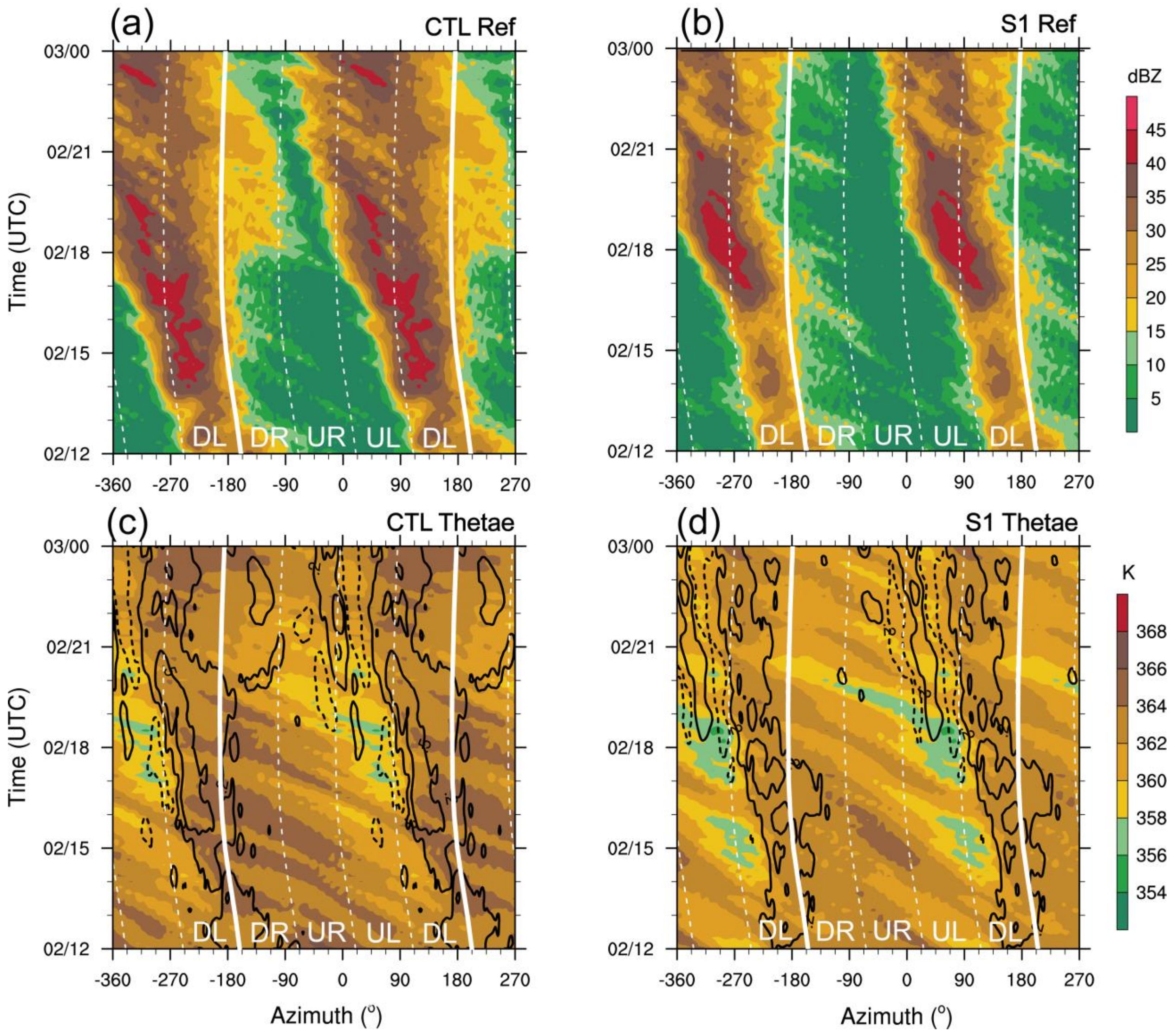

Fig. 7. (a)-(b) Time-azimuthal plot of radar reflectivity (shading, dBZ) for the CTL and S1 TCs, respectively. (c)-(d) As in (a)-(b), but for θ_e (shading, K) and vertical velocity (contours with values of –0.2, 0.2, and 0.5 m s^{-1} and negative values are dashed) for the two TCs. The radar reflectivity and θ_e are averaged within r = 20-50 km and below 500-m height. The vertical velocity is averaged within r = 20-50 km at 1-km height. The solid white line denotes the heading direction of 200-850 hPa VWS. The dashed white line marks the shear-relative quadrants, as labeled at the bottom of each panel. DR, UR, UL, and DL denote downshear-right, upshear-right, upshear-left and downshear-left quadrant, respectively.

Accepted for publication in *Journal of the Atmospheric Sciences*. DOI 10.1175/JAS-D-20-0252.1.

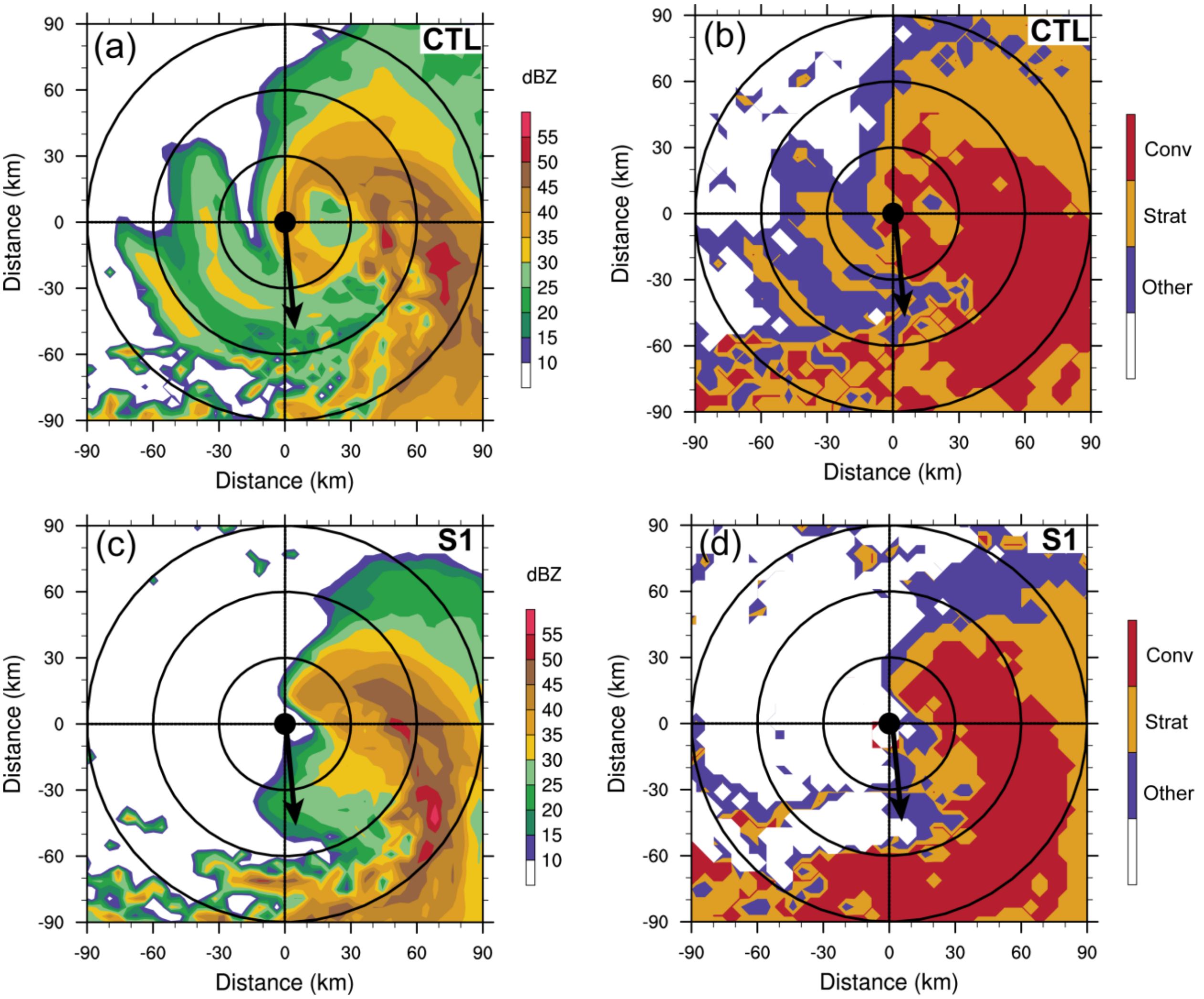

Fig. 8. Plan view of (a) radar reflectivity (shading, dBZ) at 3-km height and (b) precipitation mode at 1830 UTC 2 October. The red, yellow, and purple area in (b) denote convective, stratiform, and other type precipitation, respectively. (c)-(d) As in (a)-(b), but for S1 TC. The solid black arrow in (a)-(d) denotes the heading direction of 200-850 hPa VWS.

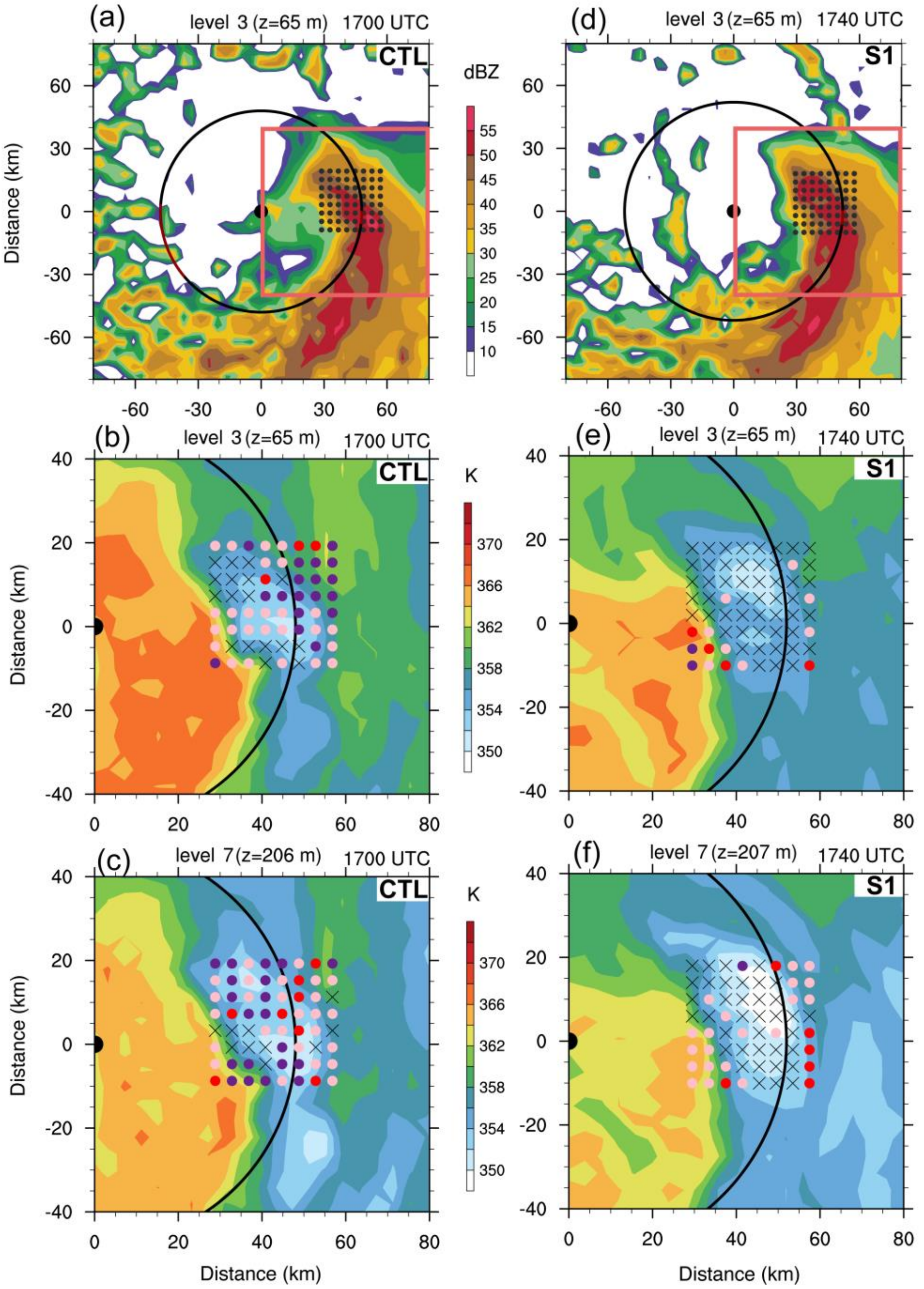

Fig. 9. Plan view of (a) radar reflectivity (shading, dBZ) at the 3rd lowest model level, θ_e (shading, K) at the (b) 3rd and (c) 7th lowest model levels at 1700 UTC 2 October for the CTL TC. (d)-(f) As in (a)-(c), but for the S1 TC at 1740 UTC. The location of the initial points of the trajectories are shown as black dots in (a) and (d), and are shown as colored dots based on the maximum height of the subsequent 4-h forward trajectory in (b)-(c) and (e)-(f). Black cross (×) denotes the boundary layer parcels with the maximum height <1.5 km. Pink, red, and violet dots denote the maximum height of these parcels within 1.5-4 km, 4-8 km, and >8 km, respectively. The large black dot at (0, 0) marks the surface TC center. The black circle represents the RMW near the surface. The orange box in (a) and (e) denotes the same area of (b)-(c) and (e)-(f), respectively. The mean height of each model level is shown in the title of each panel.

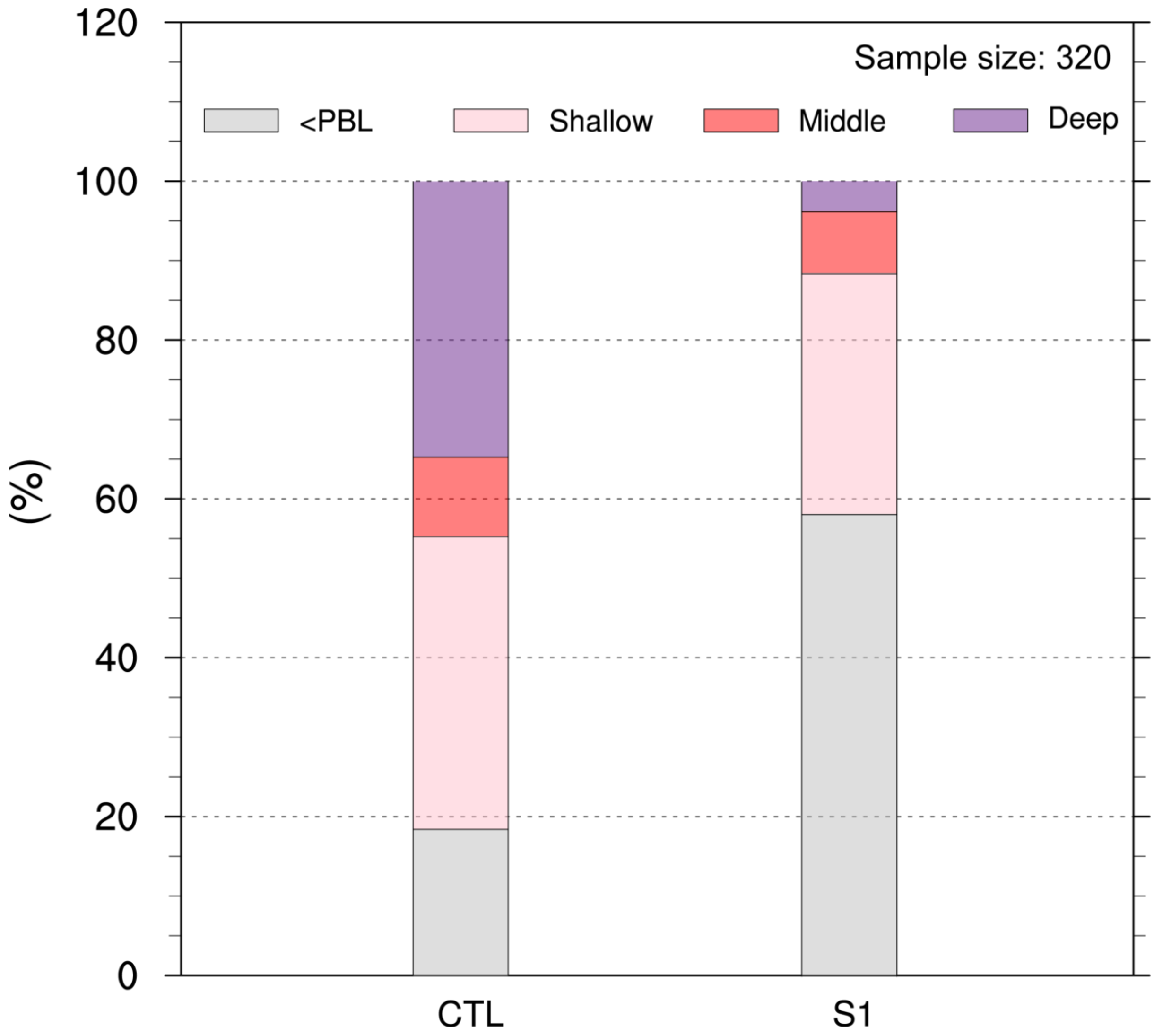

Fig. 10. Bar plot of the ratio of the track parcels that remain in the boundary layer (gray) or develop into the shallow (pink), midlevel (red) and deep (purple) convection in the CTL and S1 experiments.

Accepted for publication in *Journal of the Atmospheric Sciences*. DOI 10.1175/JAS-D-20-0252.1.

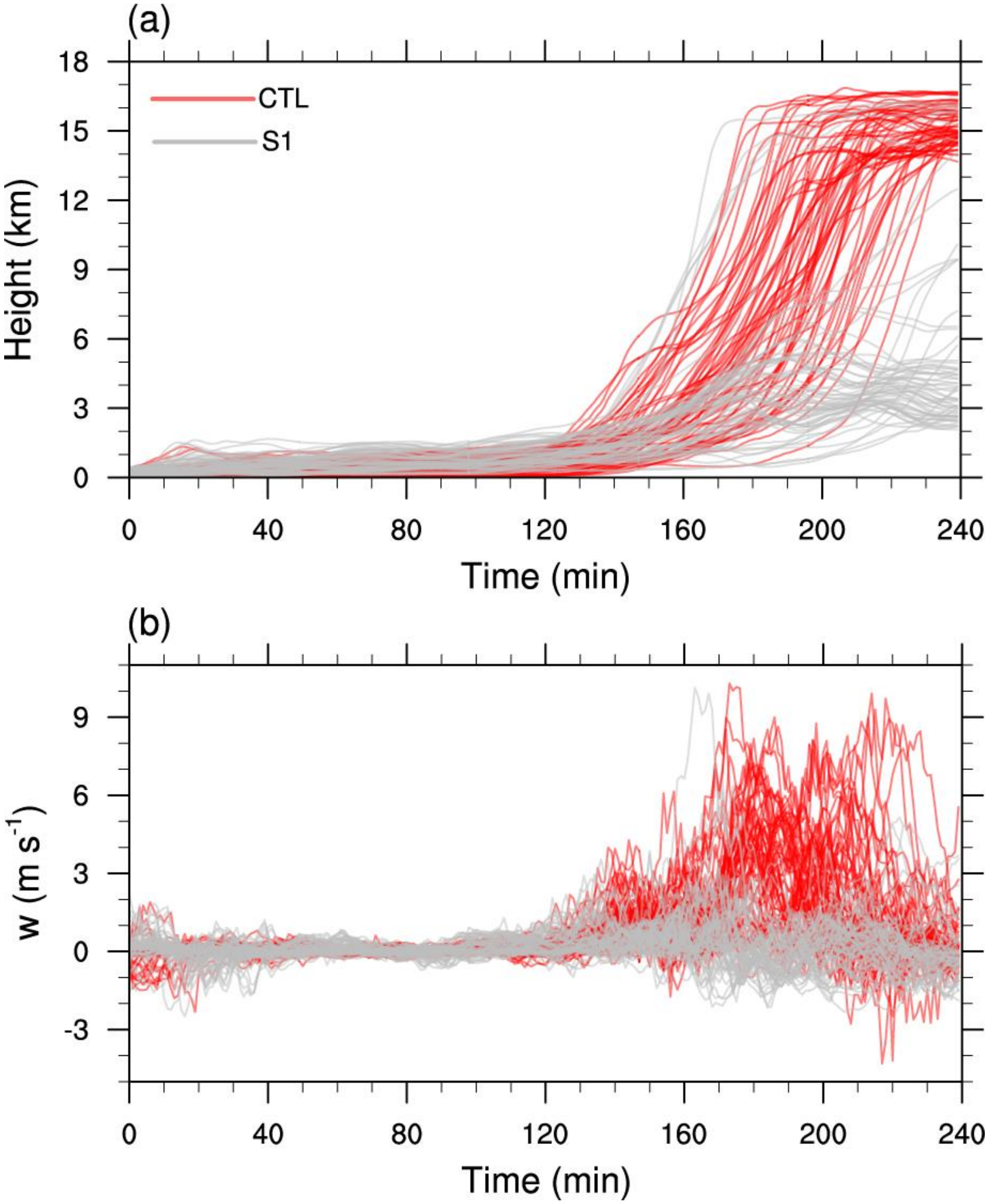

Fig. 11. The evolution of (a) parcel height (km) and (b) vertical velocity (m s^{-1}) along the 4-h trajectory for the top 20% of the parcels that are stratified by their maximum height of the 4-h trajectory. The red and gray lines denote the trajectories in CTL and S1, respectively.

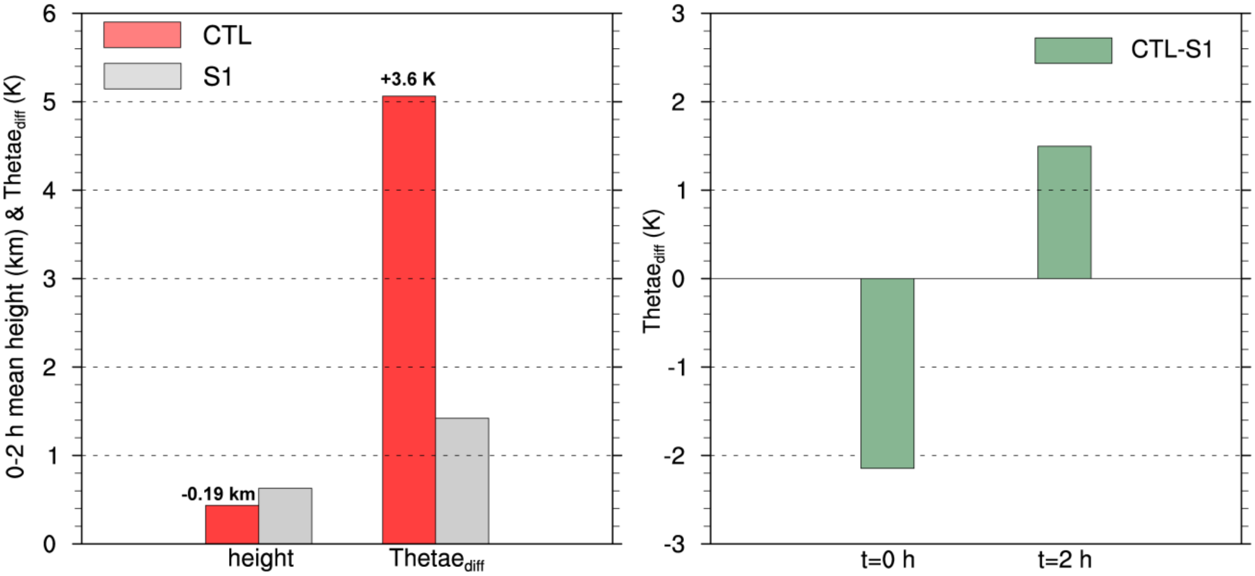

Fig. 12. Statistics for the top 20% of the parcels stratified by their maximum height of the 4-h trajectory. (a) Mean parcels height during t = 0-2 h and differences in the mean θ_e from t = 0 h to t = 2 h in CTL (red) and S1 (gray). (b) Differences in the mean θ_e between CTL and S1 (CTL–S1) at t = 0 h and t = 2 h.

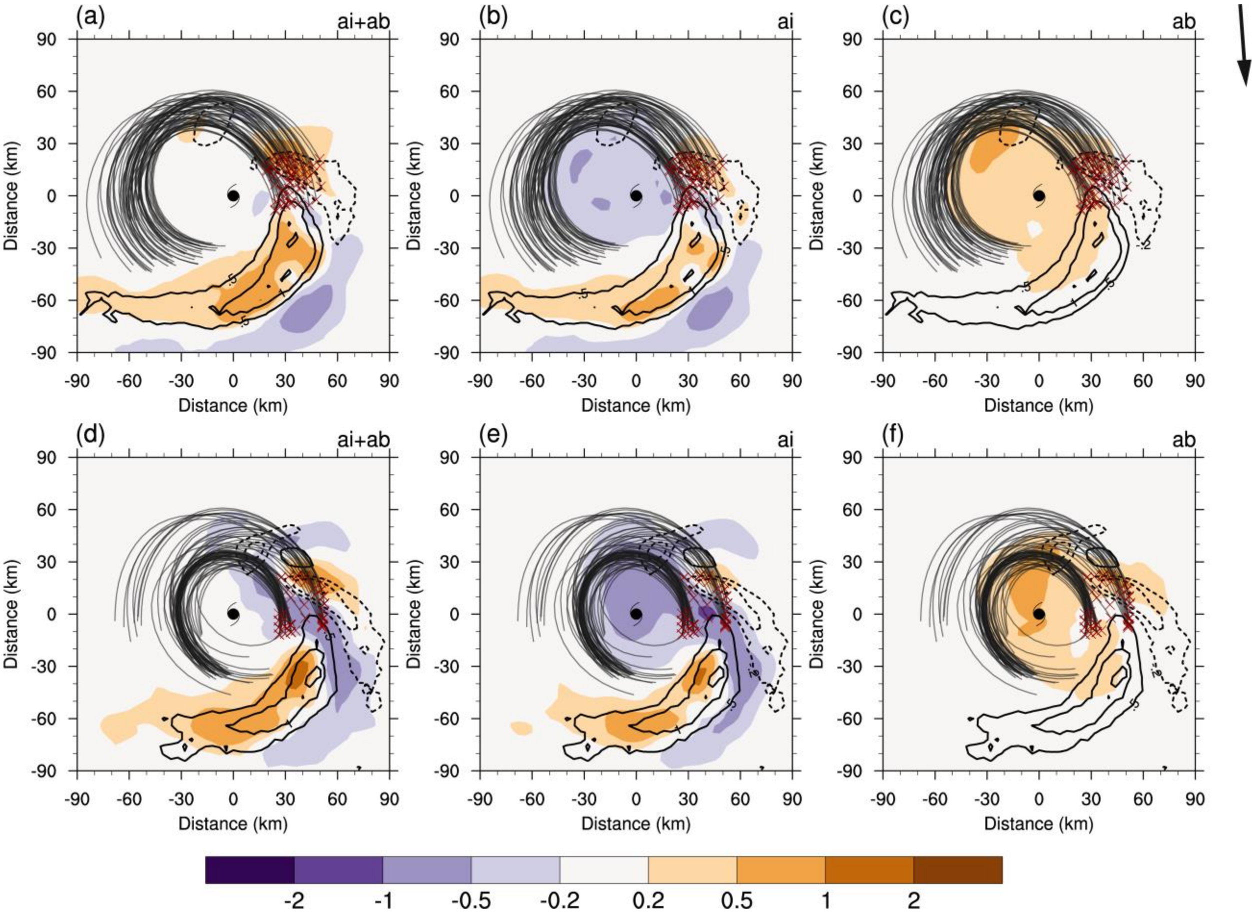

Fig. 13. Plan view of the (a) a_i (dynamic acceleration) + a_b (buoyancy acceleration) (shading, $\times 10^{-3}$ m s^{-2}), (b) a_i, and (c) a_b averaged in the lowest 1.5 km layer and over t = 0-2 h in CTL. Contours denote 1.5-km vertical velocity with values of –1, –0.5, –0.2, 0.5, 1.0, 1.5, and 2.0 m s^{-1} (negative values dashed) averaged over the same period. (d)-(f) As in (a)-(c) but in S1. The 0-2 h storm-relative trajectories of the top 20% of the parcels that are stratified by their maximum height of the 4-h trajectory are overlaid. The black arrow in the upper-right corner denotes the heading direction of the 200-850 hPa VWS. The red crosses in each panel denote the starting points of these trajectories.

Accepted for publication in *Journal of the Atmospheric Sciences*. DOI 10.1175/JAS-D-20-0252.1.

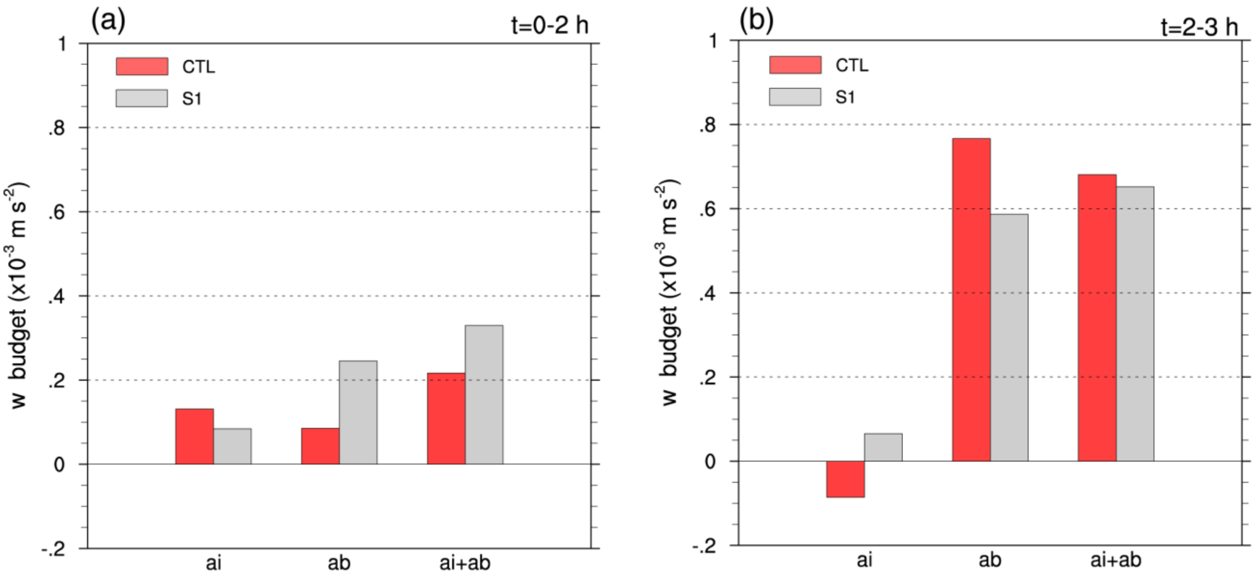

Fig. 14. Vertical velocity budget terms a_i, a_b, and $a_i + a_b$ (shading, $\times 10^{-3}$ m s^{-2}) averaged over (a) t = 0-2 h and (b) t = 2-3 h for the top 20% of the parcels that are stratified by their maximum height of the 4-h trajectory.

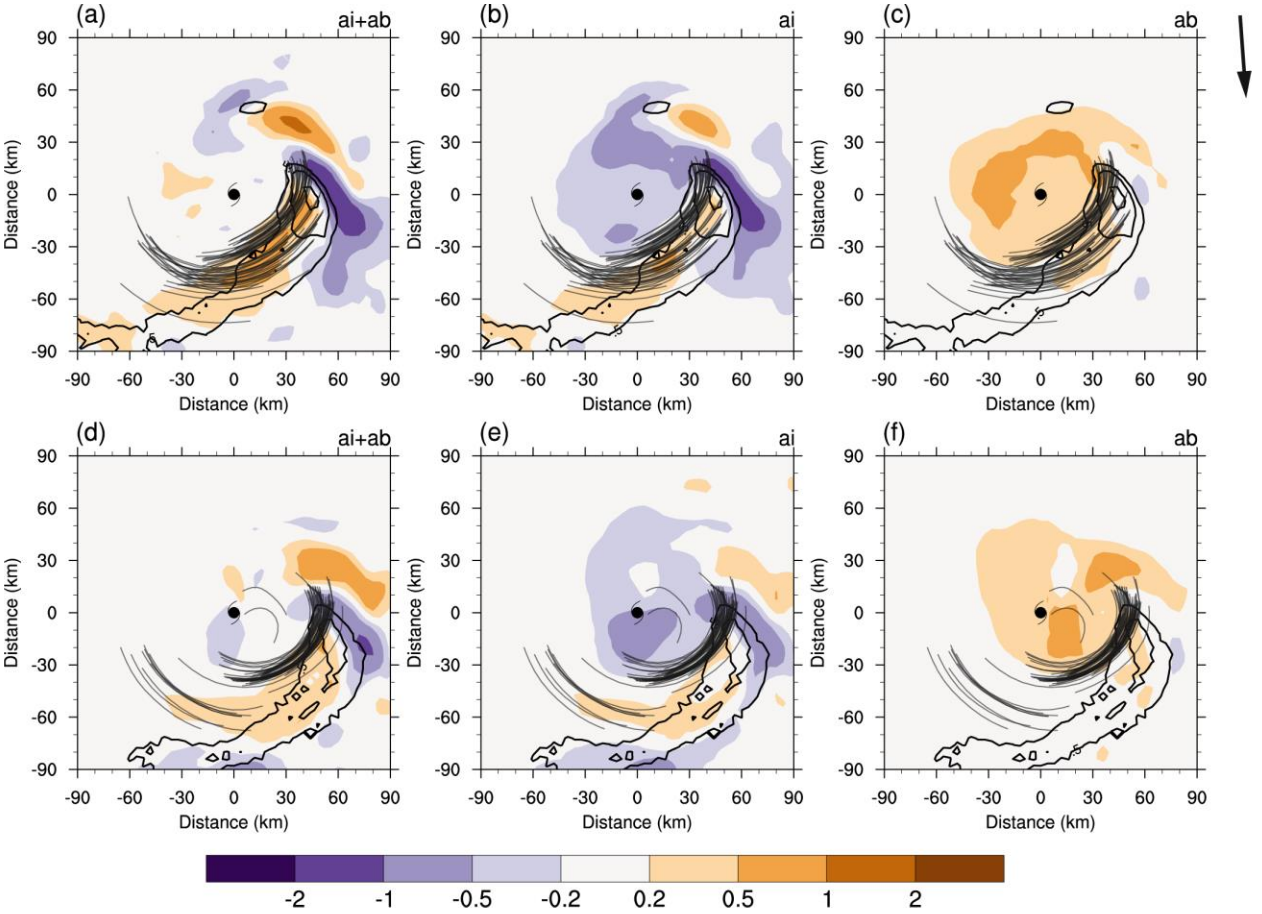

Fig. 15. As in Fig. 13, but for the results over *t*=2-3 h.

Accepted for publication in *Journal of the Atmospheric Sciences*. DOI 10.1175/JAS-D-20-0252.1.

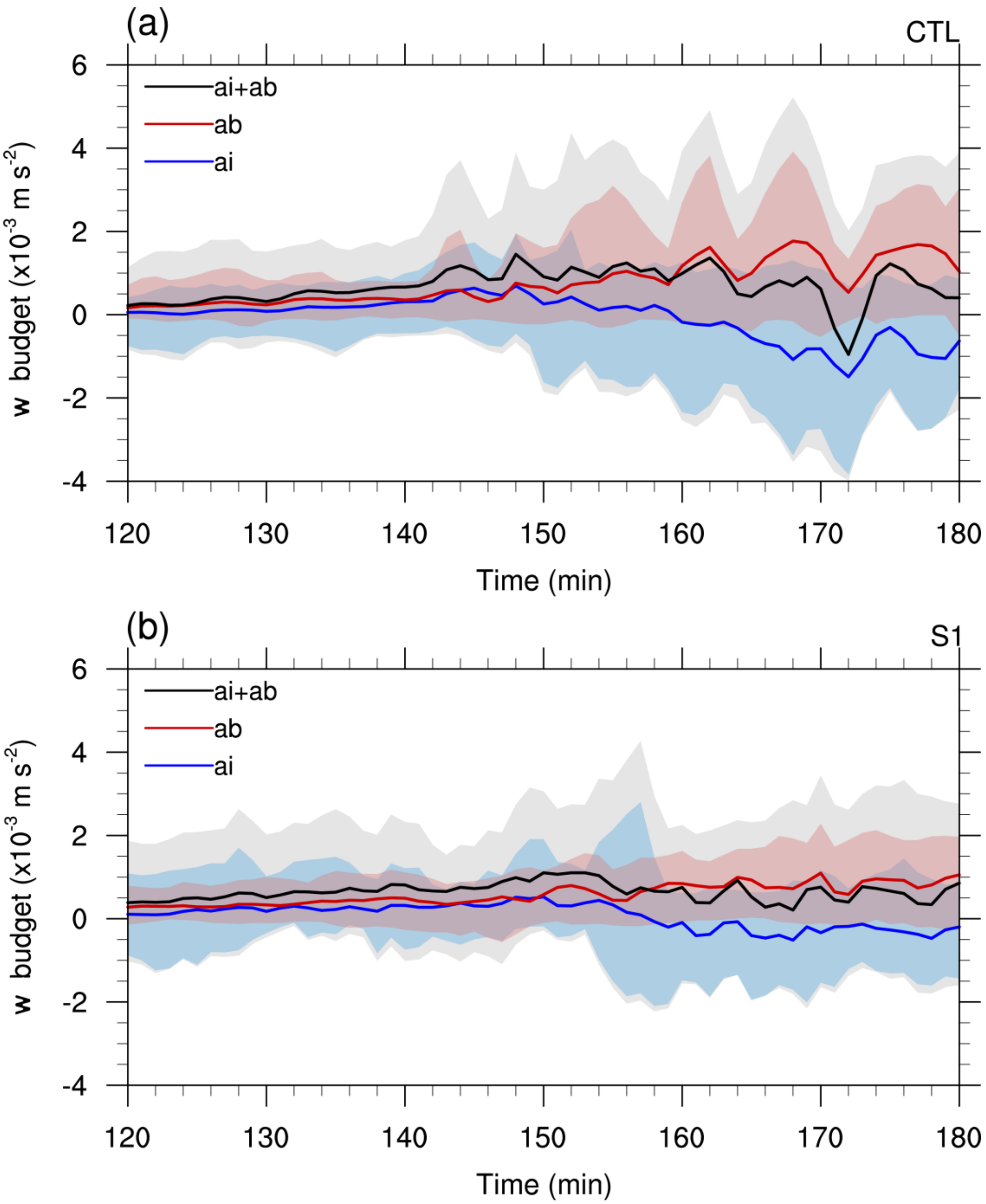

Fig. 16. Evolution of vertical velocity budget terms a_i (blue), a_b (red), and a_i+ a_b (black) over t = 2-3 h for the top 20% of the parcels that are stratified by their maximum height of the 4-h trajectory in (a) CTL and (b) S1. Lines represent mean values; shading extends from minimum to maximum at each minute. The unit of the budget terms is 10^{-3} m s^{-2}.

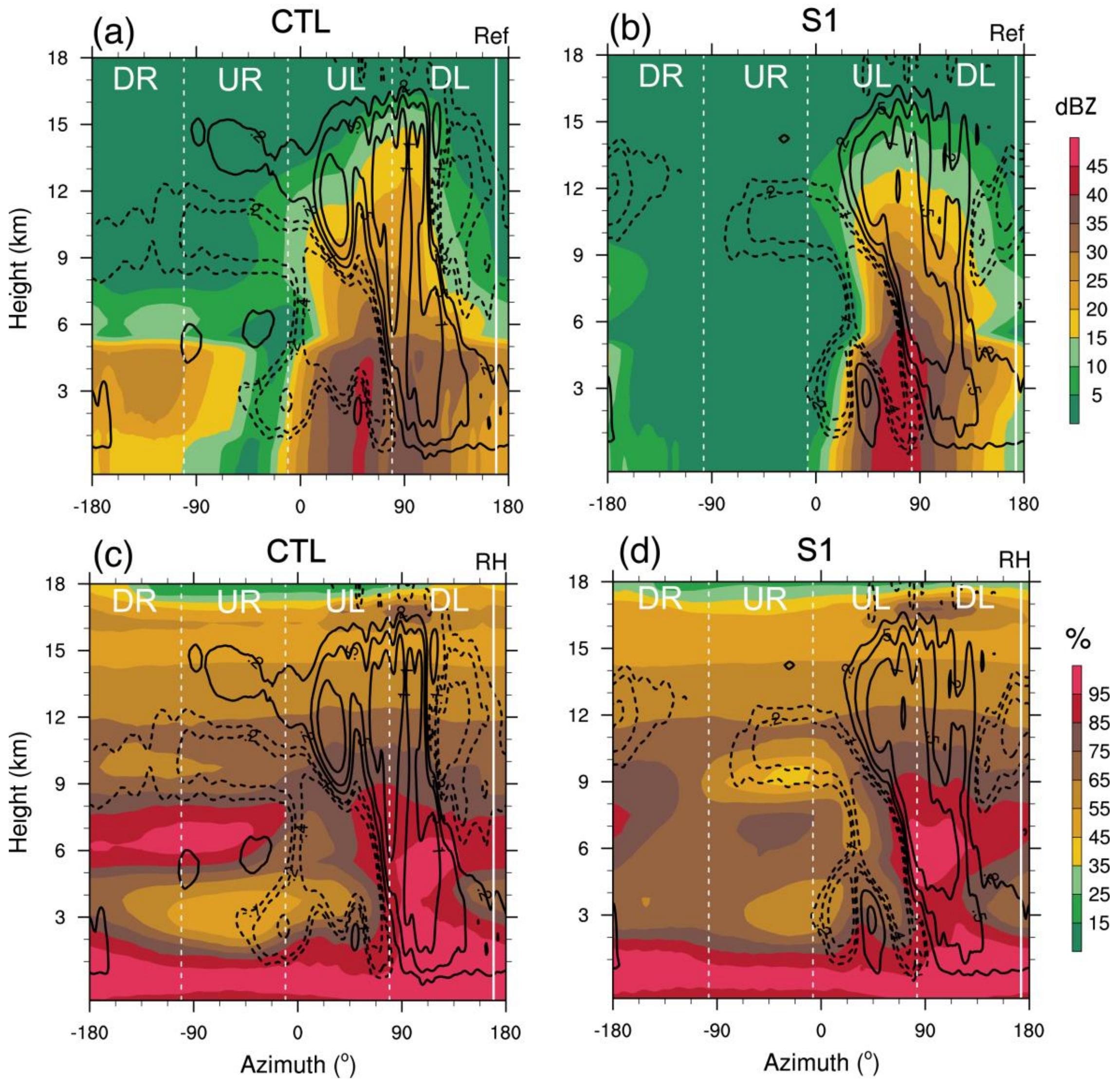

Fig. 17. Azimuthal-height plot of radar reflectivity (shading, dBZ) and vertical velocity (contours with values of –0.4, –0.2, –0.1, 0.2, 0.5, 1.0, and 2.0 $\mathrm{m\ s^{-1}}$, negative values dashed) averaged within r =20-60 km and over 1800-1850 UTC 2 October for the (a) CTL and (b) S1 TCs. (c)-(d) As in (a)-(b), but shading denotes relative humidity (%). The vertical dashed white line marks the shear-relative quadrants, as labeled at the top of each panel. DR, UR, UL, and DL denote downshear-right, upshear-right, upshear-left and downshear-left quadrant, respectively.

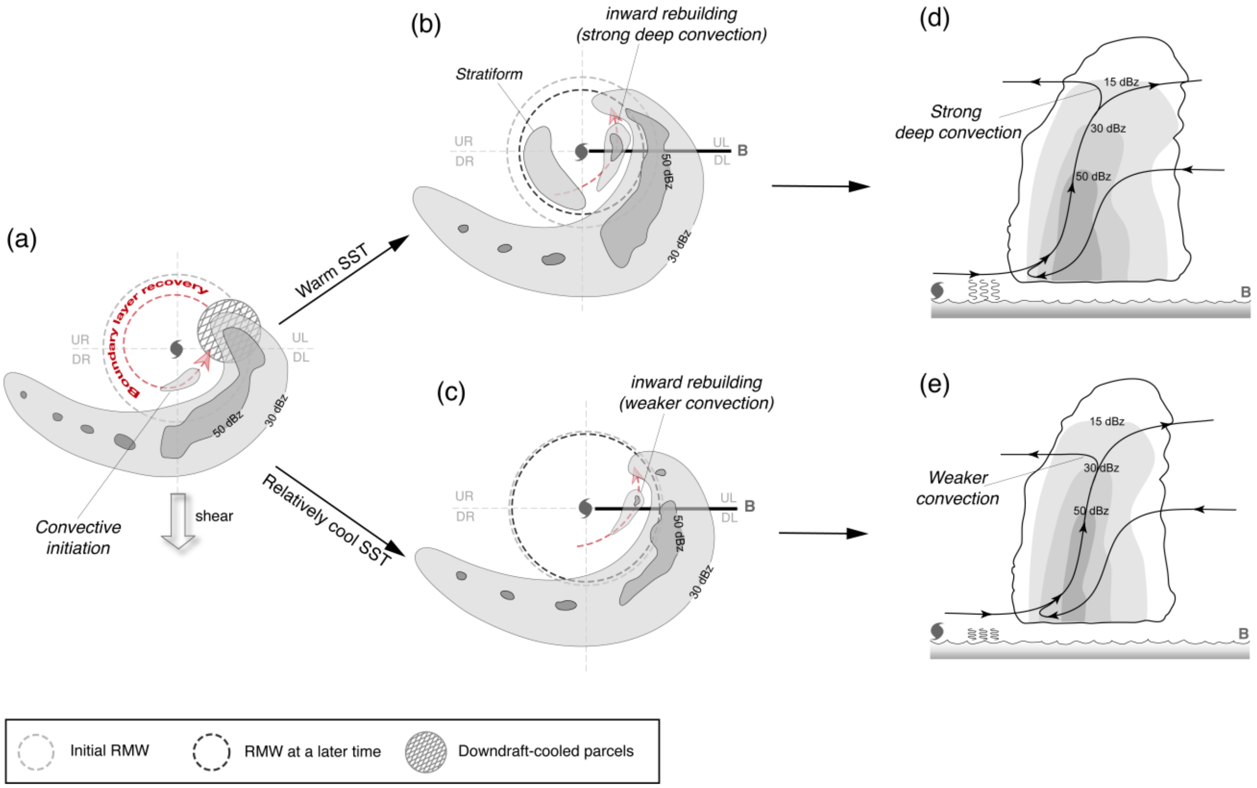

Fig. 18. Conceptual model for the inward rebuilding and precipitation symmetrization under different SSTs. (a) Plan view of the CPS that propagates into the upshear-left (UL) quadrant. Beneath the CPS, downdraft-cooled parcels in the boundary layer subsequently undergo boundary layer recovery and develop into convection during their propagation toward the downshear quadrants. (b)-(c) As in (a), but at a later time before the RI onset of the CTL TC over warm SSTs. In (b), the more efficient boundary layer recovery and more notable inward building of deep convection in UL maintain the precipitation symmetrization over warm SSTs; the stratiform in the right-of-shear semicircle in (b) indicates a nearly-saturated layer above the freezing level. (c) Over relatively cool SSTs, newly-developed convection in the inward rebuilding events is much weaker, which hinders precipitation symmetrization. Reflectivity contours represent the CPS and convective cells. The red dashed arrow in (a)-(c) denotes the trajectory along which boundary layer recovery and the subsequent inward rebuilding occur. (d)-(e) Composite vertical cross-sections of reflectivity and streamlines over warm and relatively cool SSTs, respectively. Locations of the cross sections are marked as thick black lines in (b)-(c).